

Schmidt modes carrying orbital angular momentum generated by cascaded systems pumped with Laguerre-Gaussian beams

D. Scharwald, L. Gehse, and P. R. Sharapova

Department of Physics, Paderborn University, Warburger Straße 100, 33098 Paderborn, Germany

Orbital Angular Momentum (OAM) modes are an important resource used in various branches of quantum science and technology due to their unique helical structure and countably infinite basis. Generating light that simultaneously carries high-order orbital angular momenta and exhibits quantum correlations is a challenging task. In this work, we present a theoretical approach to the generation of correlated Schmidt modes carrying OAM via parametric down-conversion (PDC) in cascaded nonlinear systems (nonlinear interferometers) pumped by Laguerre-Gaussian beams. We demonstrate how the number of generated modes and their population can be controlled by varying the pump parameters, the gain of the PDC process and the distance between the crystals. We investigate the angular displacement sensitivity of these interferometers and demonstrate that it can overcome the classical shot noise limit.

I. INTRODUCTION

Structured light has been studied extensively over the past decade and currently plays an important role in various areas of physics¹. One important type of structured light is light that carries orbital angular momentum (OAM)^{2,3}. These beams have a helical azimuthal phase dependency $e^{-il\varphi}$ with a central singularity, where φ is the azimuthal angle and $l \in \mathbb{Z}$ the OAM quantum number (topological charge number) of the mode^{1,3,4}. Due to their unique helical structure and countably infinite basis, OAM modes are an important resource for quantum communication, quantum computing, quantum information processing^{5,6} and quantum cryptography⁷. They can be generated using spatial light modulators⁸, plasmonic nanostructures⁹ or in parametric down-conversion^{6,10–12} (PDC) and four-wave mixing¹³ (FWM) processes and can be transmitted using multimode fibers^{4,14}. Recently, the transmission of OAM modes and their superpositions over long distances has been demonstrated¹⁵, which is an important element for the creation of free-space optical communication links¹⁶. In addition to the applications mentioned above, OAM modes play an important role in metrology: It has been shown that entangled OAM states can be used to improve the *angular displacement sensitivity*^{8,17,18} by a factor of $1/l$.

Thus, the generation and manipulation of correlated light carrying high-order orbital angular momenta is a vital problem. Cascaded systems of PDC processes, in particular nonlinear interferometers, constitute an important tool that can be used for these purposes since they make it possible to manipulate the set of populated OAM modes^{11,19}. Additionally, nonlinear interferometers have taken an important role in quantum metrology as they can be used to overcome the shot noise level for the phase sensitivity, which is the limit of any classical interferometer^{20–22}.

In this work, we present a theoretical framework to describe PDC and nonlinear interferometers pumped by Laguerre-Gaussian beams. Our framework is based on

the Schmidt-mode formalism developed in Ref. 11 and provides valuable analytical insights that would otherwise not be possible with rigorous methods, such as the integro-differential equations approach²³, that include time-ordering effects and can in general only be evaluated numerically.

Baghdasaryan *et al.*²⁴ have also investigated PDC with Laguerre-Gaussian pump beams to analyze the role of the Gouy phase in SPDC. For this, the SPDC state is expanded over Laguerre-Gaussian modes for the signal and idler beams. However, outside of the double-Gaussian approximation, the Schmidt modes of PDC are generally not exactly given by Laguerre-Gaussian modes^{10,11} and only look comparatively similar. Therefore, in Sec. II, we start by explicitly evaluating the spatial integral of the PDC-Hamiltonian and arrive at the two-photon amplitude (TPA) and the Schmidt decomposition for PDC with a Laguerre-Gaussian pump beam. Along the way, we will highlight similarities and differences that arise compared to the case of Gaussian pump¹¹ and illustrate the conservation of angular momentum²². Furthermore, since we present a general derivation allowing for arbitrary OAM and radial indices of the pump beam, our work can serve as a starting point for a theoretical framework with arbitrarily shaped pump beams (pump engineering), since a given pump field can always be expanded in terms of the OAM modes²⁴. This work may also provide the basis for future work on the description of PDC with Laguerre-Gaussian pump beams using the integro-differential equations approach²³.

Next, in Sec. III, we investigate the modal structure of the PDC radiation generated by pumping nonlinear interferometers with Laguerre-Gaussian beams with different OAM and radial numbers. To this end, we analyze the distribution of the weights (Schmidt eigenvalues) of the generated Schmidt modes and the output intensity profiles. In Sec. IV, we investigate the angular displacement sensitivity of these interferometers. Finally, we draw our conclusion in Sec. V.

II. THEORETICAL MODEL

A. The PDC Hamiltonian for Laguerre-Gaussian pump beams

In its general form, the Hamiltonian describing the parametric down-conversion (PDC) process is given by^{11,25,26}:

$$\hat{H} \propto \int d^3r \chi^{(2)}(\mathbf{r}) \hat{E}_p^{(+)}(\mathbf{r}, t) \hat{E}_s^{(-)}(\mathbf{r}, t) \hat{E}_i^{(-)}(\mathbf{r}, t) + \text{h.c.}, \quad (2.1)$$

where $\chi^{(2)}$ is the second order (nonlinear) susceptibility of the PDC section and $\hat{E}_j(\mathbf{r}, t)$ are the electric field operators, while the labels $j = p, s, i$ refer to the pump, signal and idler fields, respectively. In the following, we will assume $\chi^{(2)}$ to be independent of the position space coordinate vector $\mathbf{r} = [x \ y \ z]^T$. Furthermore, in this work, we restrict ourselves to monochromatic signal and idler fields, so that their field operators can be written as²⁵:

$$\hat{E}_j^{(-)}(\mathbf{r}, t) = \epsilon_j \int d^2q_j e^{-i[\mathbf{q}_j \cdot \mathbf{r}_\perp + k_{j,z}(\mathbf{q}_j, \omega_j)z - \omega_j t]} \hat{a}_j^\dagger(\mathbf{q}_j), \quad (2.2)$$

where ϵ_j is a normalization constant, $j = s, i$, and the transverse wave vector and the transverse coordinate vector are given by $\mathbf{q}_j = [k_{j,x} \ k_{j,y}]^T$ and $\mathbf{r}_\perp = [x \ y]^T$, respectively. Importantly, note that there are only two integrals over the transverse wave vectors and no integral over the frequencies ω_j . As a consequence, $k_{j,z}$ is fixed and can be written as a function of \mathbf{q}_j and ω_j , as indicated above.

The pump is described by a strong classical field with a transverse Laguerre-Gaussian profile, so that^{3,13,27}

$$E_p^{(+)}(\mathbf{r}, t) = E_0 \frac{r_\perp^{|l_p|}}{w_0^{|l_p|+1}} L_{m_p}^{|l_p|} \left(\frac{2r_\perp^2}{w_0^2} \right) e^{-\left(\frac{r_\perp}{w_0}\right)^2} \times e^{-il_p\varphi} e^{i(\mathbf{k}_p \cdot \mathbf{r} - \omega_p t)}, \quad (2.3)$$

where $r_\perp = |\mathbf{r}_\perp| = \sqrt{x^2 + y^2}$ and $\varphi = \arctan2(y, x)$ ¹ is the azimuthal angle in coordinate space. $L_{m_p}^{|l_p|}$ denotes the

Laguerre polynomials, so that $l_p \in \mathbb{Z}$ and $m_p \in \mathbb{N}_0$ are the OAM and radial quantum number of the Laguerre-Gaussian pump profile, respectively. w_0 is the width of the Gaussian term so that the full width at half maximum (FWHM) of the intensity distribution is given by $w_0\sqrt{2\ln 2}$. More specifically, w_0 can be understood as the $1/e^2$ -radius of the intensity distribution of the Gaussian term. We have therefore also assumed that the beam waist diameter is constant over the setup under consideration. This is usually satisfied if the PDC sections are sufficiently thin.

After plugging Eqs. (2.2) and (2.3) into Eq. (2.1) and assuming perfect frequency matching $\omega_p = \omega_s + \omega_i$ (neglecting time-ordering effects), the Hamiltonian can be written in the form

$$\hat{H} = i\hbar\Gamma \iint d^2q_s d^2q_i F(\mathbf{q}_s, \mathbf{q}_i) \hat{a}_s^\dagger(\mathbf{q}_s) \hat{a}_i^\dagger(\mathbf{q}_i) + \text{h.c.} \quad (2.4a)$$

where

$$F(\mathbf{q}_s, \mathbf{q}_i) = C g_{xy}(\mathbf{q}_s, \mathbf{q}_i) g_z(\mathbf{q}_s, \mathbf{q}_i) \quad (2.4b)$$

is the two-photon amplitude (TPA) of the PDC process and $C > 0$ is an l_p - and m_p -dependent normalization constant to ensure that the TPA is normalized to unity: $\iint d^2q_s d^2q_i |F(\mathbf{q}_s, \mathbf{q}_i)|^2 = 1$. The newly introduced constant $\Gamma = \epsilon_0 \frac{\chi^{(2)}}{3} \frac{1}{C} \epsilon_s \epsilon_i E_0$ is the theoretical gain parameter. We have factorized the TPA so that the function g_{xy} contains the spatial integrals over the (transverse) xy -plane and g_z contains the integral along the z -axis, both of which originate from the PDC Hamiltonian in Eq. (2.1).

B. Evaluation of the transverse spatial integral

The integral over the xy -plane of the nonlinear medium corresponds to the Fourier transform of the Laguerre-Gaussian envelope. In polar coordinates, $\mathbf{q}_j \equiv (q_j, \phi_j)$ (with $j = s, i$) and $\mathbf{r}_\perp \equiv (r, \varphi)$, this integral takes the form:

$$g_{xy}(q_s, q_i, \phi_s, \phi_i) = \int dr \int d\varphi \left(\frac{r}{w_0} \right)^{|l_p|+1} L_{m_p}^{|l_p|} \left(\frac{2r^2}{w_0^2} \right) e^{-\left(\frac{r}{w_0}\right)^2} e^{-il_p\varphi} e^{-ir[q_s \cos(\varphi - \phi_s) + q_i \cos(\varphi - \phi_i)]}. \quad (2.5)$$

Since the last exponent is a superposition of weighted cosine terms, it can be rewritten in terms of a single sine function^{28, p. 84}:

$$q_s \cos(\varphi - \phi_s) + q_i \cos(\varphi - \phi_i) = \xi(q_s, q_i, \phi_s, \phi_i) \sin[\varphi + \psi(q_s, q_i, \phi_s, \phi_i)], \quad (2.6a)$$

¹ Throughout this work, we will use the two-argument arctangent function $\arctan2$ for clarity, when appropriate.

where

$$\xi(q_s, q_i, \phi_s, \phi_i) = \sqrt{q_s^2 + q_i^2 + 2q_s q_i \cos(\phi_s - \phi_i)}, \quad (2.6b)$$

$$\psi(q_s, q_i, \phi_s, \phi_i) = \arctan 2(q_s \cos \phi_s + q_i \cos \phi_i, q_s \sin \phi_s + q_i \sin \phi_i). \quad (2.6c)$$

Note that $\xi = |\mathbf{q}_p|^{24}$. The transverse integral can then be rewritten in a more simple form:

$$g_{xy}(q_s, q_i, \phi_s, \phi_i) = \int dr \left(\frac{r}{w_0} \right)^{|l_p|+1} L_{m_p}^{|l_p|} \left(\frac{2r^2}{w_0^2} \right) e^{-\left(\frac{r}{w_0}\right)^2} \int_0^{2\pi} d\varphi e^{i(-r\xi \sin(\varphi+\psi) - l_p \varphi)}. \quad (2.7)$$

The integration over the polar angle φ can be performed by using the definition of the Bessel functions of the first kind J_n ^{24,29, p. 20} and can be evaluated as:

$$\int_0^{2\pi} d\varphi e^{i(-r\xi \sin(\varphi+\psi) - l_p \varphi)} = 2\pi [-\text{sgn}(l_p)]^{l_p} e^{il_p \psi} J_{|l_p|}(r\xi), \quad (2.8)$$

where sgn is the sign function. The remaining integral over the radial coordinate r then becomes a Hankel transformation integral of order $|l_p|$ ^{28, p. 768}:

$$g_{xy}(q_s, q_i, \phi_s, \phi_i) = 2\pi [-\text{sgn}(l_p)]^{l_p} e^{il_p \psi} \int_0^\infty dr \left(\frac{r}{w_0} \right)^{|l_p|+1} L_{m_p}^{|l_p|} \left(\frac{2r^2}{w_0^2} \right) e^{-\left(\frac{r}{w_0}\right)^2} J_{|l_p|}(r\xi). \quad (2.9)$$

Substituting $x = \sqrt{2}r/w_0$, this integral can be directly evaluated using the following Hankel transform integral formula^{30, p. 42}:

$$\int_0^\infty dx x^{\nu+\frac{1}{2}} e^{-\frac{1}{2}x^2} L_n^\nu(x^2) J_\nu(xy) (xy)^{\frac{1}{2}} = (-1)^n e^{-\frac{1}{2}y^2} y^{\nu+\frac{1}{2}} L_n^\nu(y^2), \quad (2.10)$$

which is valid for $\text{Re}(\nu) > -1$ and $y > 0$. Finally, the function g_{xy} is given by:

$$g_{xy}(q_s, q_i, \phi_s, \phi_i) = 2\pi [\text{sgn}(l_p)]^{|l_p|} (-1)^{l_p+m_p} \left(\frac{w_0}{2} \right)^{|l_p|+1} e^{-\left(\frac{w_0\xi}{2}\right)^2} e^{il_p \psi} \xi^{|l_p|} L_{m_p}^{|l_p|} \left(\frac{(w_0\xi)^2}{2} \right). \quad (2.11)$$

C. Separation of the signal and idler variables

It can be shown that $\psi(q_s, q_i, \phi_s, \phi_i)$ defined in Eq. (2.6c) and appearing in the exponential function in Eq. (2.11) and, therefore, the entire TPA, cannot simply be written in terms of the signal-idler angle difference $\phi_s - \phi_i$. This means that the results derived in Ref. 11 for the Gaussian pump cannot be directly applied for the Laguerre-Gaussian beam because the one-dimensional Fourier decomposition as given in Eq. (3) therein cannot be applied to the TPA derived above. However, as will be shown below, it is possible to find a similar decomposition for the TPA derived in this work.

To see this, first, note that

$$\sin(\psi) = \frac{q_s \cos(\phi_s) + q_i \cos(\phi_i)}{\xi}, \quad (2.12a)$$

$$\cos(\psi) = \frac{q_s \sin(\phi_s) + q_i \sin(\phi_i)}{\xi}. \quad (2.12b)$$

Using Euler's formula for the exponential function and taking into account Eqs. (2.12a) and (2.12b), the function

$e^{il_p \psi}$ can be rewritten as²

$$e^{il_p \psi} = \left(\frac{i \text{sgn}(l_p)}{\xi} \right)^{|l_p|} W(q_s, q_i, \phi_s - \phi_i) e^{-il_p \phi_i}, \quad (2.13a)$$

where

$$W(q_s, q_i, \phi_s - \phi_i) = \left[q_s e^{-i \text{sgn}(l_p)(\phi_s - \phi_i)} + q_i \right]^{|l_p|}. \quad (2.13b)$$

Here, we have chosen to factor out the exponential term containing the idler angular variable ϕ_i from W . However, it is also possible to instead factor out the exponential term containing ϕ_s or both. The TPA can then be

² To see this, write $l_p = |l_p| \text{sgn}(l_p)$, apply Euler's formula to the exponential term in $[\exp(i \text{sgn}(l_p) \psi)]^{|l_p|}$, then Eqs. (2.12a) and (2.12b), use the fact that \cos and \sin are even and odd functions in their arguments, respectively, to multiply the argument with $\text{sgn}(l_p)$ when necessary and finally apply Euler's formula backwards.

combined as:

$$F(q_s, q_i, \phi_s, \phi_i) = R(q_s, q_i, \phi_s - \phi_i) e^{-il_p \phi_i}, \quad (2.14)$$

with the newly defined function

$$\begin{aligned} R(q_s, q_i, \phi_s - \phi_i) &= 2\pi C (-1)^{l_p+m_p} i^{|l_p|} \left(\frac{w_0}{2}\right)^{|l_p|+1} \\ &\times L_{m_p}^{|l_p|} \left(\frac{(w_0 \xi)^2}{2}\right) e^{-\left(\frac{w_0 \xi}{2}\right)^2} \\ &\times \left[q_s e^{-i \operatorname{sgn}(l_p)(\phi_s - \phi_i)} + q_i \right]^{|l_p|} \\ &\times g_z(q_s, q_i, \phi_s - \phi_i), \end{aligned} \quad (2.15)$$

which depends only on the signal-idler angle difference $\phi_s - \phi_i$. Intuitively, this result for R is plausible, since Laguerre-Gaussian functions are fixed points/eigenfunctions of the Fourier transform³¹. The normalization constant C must be chosen so that $\iiint dq_s dq_i d\phi q_s q_i |R(q_s, q_i, \phi)|^2 = 1/(2\pi)$, which is a consequence of the fact that we write R in terms of the signal-idler angle difference ϕ .

As mentioned above, the full TPA F cannot be written purely in terms of $\phi_s - \phi_i$. Therefore, we apply the one-dimensional Fourier expansion only to R :

$$R(q_s, q_i, \phi_s - \phi_i) = \frac{1}{2\pi} \sum_{n=-\infty}^{\infty} \chi_n(q_s, q_i) e^{-in(\phi_s - \phi_i)}. \quad (2.16)$$

The Fourier coefficients $\chi_n(q_s, q_i)$ can be obtained by computing the Fourier coefficient integral:

$$\chi_n(q_s, q_i) = \int_0^{2\pi} d(\phi_s - \phi_i) R(q_s, q_i, \phi_s - \phi_i) e^{in(\phi_s - \phi_i)}. \quad (2.17)$$

Plugging the Fourier decomposition [Eq. (2.16)] into Eq. (2.14), one can obtain the expansion of the full TPA in terms of the coefficients $\chi_n(q_s, q_i)$ as

$$F(q_s, q_i, \phi_s, \phi_i) = \frac{1}{2\pi} \sum_n \chi_n(q_s, q_i) e^{-in\phi_s} e^{-i(l_p-n)\phi_i}. \quad (2.18)$$

For $l_p = 0$, the regular Fourier decomposition over the angle difference is recovered¹¹, resulting in perfectly anti-correlated OAM for the signal and idler photons. The normalization condition for the TPA now implies $\sum_n \iint dq_s dq_i q_s q_i |\chi_n(q_s, q_i)|^2 = 1$ (corresponding to *Parseval's theorem*^{28, p. 637}).

The Schmidt decomposition for the expansion coefficients reads¹¹:

$$\chi_n(q_s, q_i) = \sum_{m=0}^{\infty} \sqrt{\lambda_{mn}} \frac{u_{mn}(q_s)}{\sqrt{q_s}} \frac{v_{mn}(q_i)}{\sqrt{q_i}}, \quad (2.19)$$

where λ_{mn} are the Schmidt eigenvalues and u_{mn} and v_{mn} are the eigenfunctions. The properties of the Schmidt decomposition ensure that the radial mode functions u_{mn} and v_{mn} fulfill the following orthonormality conditions:

$$\int dq_s u_{mn}(q_s) u_{kn}^*(q_s) = \delta_{mk}, \quad (2.20a)$$

$$\int dq_i v_{mn}(q_i) v_{kn}^*(q_i) = \delta_{mk}. \quad (2.20b)$$

Furthermore, the normalization condition of the TPA now requires $\sum_{m,n} \lambda_{mn} = 1$.

Finally, the TPA can be written in the following form:

$$F(q_s, q_i, \phi_s, \phi_i) = \frac{1}{2\pi} \sum_{m,n} \sqrt{\lambda_{mn}} \frac{u_{mn}(q_s)}{\sqrt{q_s}} \frac{v_{mn}(q_i)}{\sqrt{q_i}} e^{-in\phi_s} e^{-i(l_p-n)\phi_i}. \quad (2.21)$$

From this expression, it can be seen that for the fixed summation indices m and n , the signal and idler photons have different OAM, namely, n and $l_p - n$, respectively. This form of the TPA allows us to introduce the spatially broadband Schmidt operators \hat{A}_{mn} , \hat{B}_{mn} and diagonalize the full Hamiltonian:

$$\hat{H} = i\hbar\Gamma \sum_{m,n} \sqrt{\lambda_{mn}} \left(\hat{A}_{mn}^\dagger \hat{B}_{mn}^\dagger - \hat{A}_{mn} \hat{B}_{mn} \right), \quad (2.22)$$

where the Schmidt operators are defined as

$$\hat{A}_{mn}^\dagger = \frac{1}{\sqrt{2\pi}} \int d^2 q_s \frac{u_{mn}(q_s)}{\sqrt{q_s}} e^{-in\phi_s} \hat{a}_s^\dagger(\mathbf{q}_s), \quad (2.23a)$$

$$\hat{B}_{mn}^\dagger = \frac{1}{\sqrt{2\pi}} \int d^2 q_i \frac{v_{mn}(q_i)}{\sqrt{q_i}} e^{-i(l_p-n)\phi_i} \hat{a}_i^\dagger(\mathbf{q}_i). \quad (2.23b)$$

Note that since we work in polar coordinates, the area element is given by $d^2 q_j = q_j dq_j d\phi_j$ for $j = s, i$.

From the expressions of the Schmidt operators one can see that the creation operator \hat{A}_{mn}^\dagger creates a spatially

multimode signal photon over the plane-wave basis with OAM n , while the creation operator \hat{B}_{mn}^\dagger creates an idler photon with the complementary OAM of $l_p - n$. Together, these two operators always create two photons in their corresponding Schmidt modes while conserving the OAM of the pump photons: $n + (l_p - n) = l_p$.

D. Symmetries and commutation relations

For several important systems, the function g_z containing the spatial z -axis integral have the symmetry property:

$$g_z(q_s, q_i, \phi_s - \phi_i) = g_z(q_s, q_i, \phi_i - \phi_s), \quad (2.24a)$$

which also always holds for the function ξ defined in Eq. (2.6b):

$$\xi(q_s, q_i, \phi_s - \phi_i) = \xi(q_s, q_i, \phi_i - \phi_s). \quad (2.24b)$$

In other words, these two functions are even in the angle difference $\phi_s - \phi_i$. Additionally, these functions are also 2π -periodic in the angle difference.

In this work, we will restrict ourselves to analyzing PDC from single crystals and from two-crystal setups [SU(1,1) interferometers]. Furthermore, we will only consider degenerate type-I PDC, where the signal and idler photons have the same frequency and polarization. From the concrete expressions of g_z for these systems, see Eqs. (3.1) and (3.5) below³, it can be directly seen that the symmetry property in Eq. (2.24a) holds. Additionally, this property also holds for the TPA derived in Sec. IV since the dependencies on \mathbf{q}_s and \mathbf{q}_i can be reduced to those of a single crystal.

Since we are working in the frequency-degenerate regime, the refractive indices for the signal and idler beam are the same. As a consequence, for the fixed phase difference ϕ , the function g_z is invariant under the exchange of the signal and idler variables, which also (always) holds for ξ :

$$g_z(q_s, q_i, \phi) = g_z(q_i, q_s, \phi), \quad (2.25a)$$

$$\xi(q_s, q_i, \phi) = \xi(q_i, q_s, \phi). \quad (2.25b)$$

Note that these properties do not apply to R defined in Eq. (2.15) due to the presence of the factor W , as defined in Eq. (2.13b). However, for this term,

$$e^{il_p(\phi_s - \phi_i)} W(q_s, q_i, \phi_s - \phi_i) = W(q_i, q_s, \phi_i - \phi_s). \quad (2.26)$$

Combined, Eqs. (2.13b) and (2.24)–(2.26) imply

$$e^{il_p(\phi_s - \phi_i)} R(q_s, q_i, \phi_s - \phi_i) = R(q_i, q_s, \phi_i - \phi_s). \quad (2.27)$$

Applying this to the inverse transform of the Fourier decomposition given in Eq. (2.16) reveals:

$$\chi_{l_p - n}(q_s, q_i) = \chi_n(q_i, q_s). \quad (2.28)$$

Due to this relation, the Schmidt decomposition components have the following helpful properties:

$$\lambda_{m, l_p - n} = \lambda_{mn}, \quad (2.29a)$$

$$u_{m, l_p - n} = v_{mn}, \quad (2.29b)$$

$$v_{m, l_p - n} = u_{mn}, \quad (2.29c)$$

which can also be applied to the Schmidt operators. Due to the fact that we are working in the degenerate regime, we obtain:

$$\hat{A}_{m, l_p - n}^\dagger = \hat{B}_{mn}^\dagger, \quad (2.30a)$$

$$\hat{B}_{m, l_p - n} = \hat{A}_{mn}. \quad (2.30b)$$

Furthermore, note that the full TPA is invariant under the $\mathbf{q}_s \leftrightarrow \mathbf{q}_i$ exchange:

$$F(q_s, q_i, \phi_s, \phi_i) = F(q_i, q_s, \phi_i, \phi_s), \quad (2.31)$$

which can be seen directly from Eqs. (2.14) and (2.27) and reflects the degeneracy of the PDC process.

Using the definition of the Schmidt operators [Eqs. (2.23a) and (2.23b)] it can be seen that the commutation relation of the Schmidt operators \hat{A}_{mn} and \hat{B}_{mn} with their respective hermitian conjugates are:

$$[\hat{A}_{mn}, \hat{A}_{kl}^\dagger] = \delta_{mk} \delta_{nl}, \quad (2.32a)$$

$$[\hat{B}_{mn}, \hat{B}_{kl}^\dagger] = \delta_{mk} \delta_{nl}. \quad (2.32b)$$

These coincide with the relations already found for the case $l_p = 0$ in Ref. 11. From the connections between the Schmidt operators given in Eqs. (2.30a) and (2.30b) it is immediately clear that the commutation relation between the signal and idler Schmidt operators is given by

$$[\hat{A}_{mn}, \hat{B}_{kl}^\dagger] = \delta_{mk} \delta_{n, l_p - l}, \quad (2.32c)$$

which reduces to the result found in Ref. 11 for $l_p = 0$, as expected.

It should be emphasized that the labeling of “signal” and “idler” photons is now, due to the degeneracy of the process under consideration, only meaningful in the sense that the photons of each signal-idler pair carry complementary orbital angular momenta with respect to the pump. This can also be seen from the symmetry properties given in Eqs. (2.28), (2.29a)–(2.29c) and (2.30): Swapping the OAM index n with its complementary value $l_p - n$ is equivalent to switching between the signal and idler subsystems.

³ Note that the symmetry properties of g_z shown in Eqs. (2.24a) and (2.25a) also hold for the exact expressions without the Fresnel approximation, see Eqs. (3.2) and (3.3) and the surrounding text. Additionally, note that $k_{p,z}(\mathbf{q}_s, \mathbf{q}_i) = \sqrt{|\mathbf{k}_p|^2 - \xi^2(q_s, q_i, \phi_s - \phi_i)}$, where $|\mathbf{k}_p|$ is a constant depending on the pump frequency and refractive index.

If we had assumed that the signal and idler plane-wave operators describe distinguishable photons, for example due to different polarizations or frequencies, A_{mn} and B_{kl}^\dagger would commute: $[A_{mn}, B_{kl}^\dagger] = 0$. However, since this is not the case in our consideration, the two Schmidt-mode operators commute only when they differ in at least one of the two indices.

E. Equations of motion and intensity spectrum

Using the commutation relations for the Schmidt operators [Eqs. (2.32a) and (2.32b)], one can obtain their equations of motion in the Heisenberg picture:

$$\frac{d\hat{A}_{mn}}{dt} = \Gamma\sqrt{\lambda_{mn}} \left(\hat{A}_{m, l_p - n}^\dagger + \hat{B}_{mn}^\dagger \right) = 2\Gamma\sqrt{\lambda_{mn}} \hat{B}_{mn}^\dagger, \quad (2.33a)$$

$$\frac{d\hat{B}_{mn}^\dagger}{dt} = \Gamma\sqrt{\lambda_{mn}} \left(\hat{A}_{mn} + \hat{B}_{m, l_p - n} \right) = 2\Gamma\sqrt{\lambda_{mn}} \hat{A}_{mn}, \quad (2.33b)$$

where the relationships between the Schmidt operators given in Eqs. (2.30a) and (2.30b) have been used in the second step.

The solutions to this set of differential equations are the well-known Bogoliubov transforms¹¹:

$$\hat{A}_{mn}^{\text{out}} = \hat{A}_{mn}^{\text{in}} \cosh(G\sqrt{\lambda_{mn}}) + \left(\hat{B}_{mn}^{\text{in}} \right)^\dagger \sinh(G\sqrt{\lambda_{mn}}), \quad (2.34a)$$

$$\hat{B}_{mn}^{\text{out}} = \hat{B}_{mn}^{\text{in}} \cosh(G\sqrt{\lambda_{mn}}) + \left(\hat{A}_{mn}^{\text{in}} \right)^\dagger \sinh(G\sqrt{\lambda_{mn}}), \quad (2.34b)$$

where $G = \int dt 2\Gamma$ is the theoretical parametric gain and the integral is taken over the interaction time. The operators denoted with the ⁱⁿ superscript are the input Schmidt operators at the beginning of the interaction (at the input of the PDC section), while operators on the right hand side, denoted with ^{out}, are the output operators at the end of the interaction (at the output of the PDC section).

The commutators of the plane-wave annihilation operator and the Schmidt operators are given by

$$[\hat{a}(\mathbf{q}), \hat{A}_{mn}^\dagger] = \frac{1}{\sqrt{2\pi}} \frac{u_{mn}(q)}{\sqrt{q}} e^{-in\phi}, \quad (2.35a)$$

$$[\hat{a}(\mathbf{q}), \hat{B}_{mn}^\dagger] = \frac{1}{\sqrt{2\pi}} \frac{v_{mn}(q)}{\sqrt{q}} e^{-i(l_p - n)\phi}. \quad (2.35b)$$

Note that these hold regardless of whether $\hat{a}(\mathbf{q})$ belongs to the signal or idler subsystem due to the degeneracy condition mentioned in Sec. IID, which is also why the index j referring to either the signal or idler subsystem was dropped [here and in the following, $\mathbf{q} \equiv (q, \phi)$]. If the signal and idler plane-wave operators were describing distinguishable photons, the commutators given in Eqs. (2.35a) and (2.35b) would vanish if the plane-wave annihilation operator corresponds to the opposite subsystem as the Schmidt operator.

Using these commutation relations, one can obtain the equations of motion for the plane-wave annihilation operator using the Hamiltonian given in Eq. (2.22):

$$\frac{d\hat{a}(\mathbf{q})}{dt} = \frac{2\Gamma}{\sqrt{2\pi}} \sum_{m,n} \sqrt{\lambda_{mn}} \frac{u_{mn}(q)}{\sqrt{q}} e^{-in\phi} \hat{B}_{mn}^\dagger, \quad (2.36)$$

where we have shifted a summation index and used Eqs. (2.29a)–(2.29c) and (2.30a) so that only B_{mn}^\dagger remains in the result.

By using Eqs. (2.33a) and (2.34a), the solution to the differential equation (2.36) can be found:

$$\hat{a}^{\text{out}}(\mathbf{q}) = \hat{a}^{\text{in}}(\mathbf{q}) + \frac{1}{\sqrt{2\pi}} \sum_{m,n} \frac{u_{mn}(q)}{\sqrt{q}} e^{-in\phi} \left\{ \hat{A}_{mn}^{\text{in}} \left[\cosh(G\sqrt{\lambda_{mn}}) - 1 \right] + \left(\hat{B}_{mn}^{\text{in}} \right)^\dagger \sinh(G\sqrt{\lambda_{mn}}) \right\}, \quad (2.37)$$

where the plane-wave operators with the ⁱⁿ and ^{out} superscripts are the input and output operators of the PDC section, respectively, analogously to the Schmidt operators with the same superscripts. Note that the input Schmidt mode operators depend on the input plane-wave operators.

Using the definition of the plane-wave photon number operator, $\hat{N}(\mathbf{q}) = [\hat{a}^{\text{out}}(\mathbf{q})]^\dagger \hat{a}^{\text{out}}(\mathbf{q})$, it is easy to see that the intensity distribution (mean photon number distribution)

is given by:

$$\langle \hat{N}(\mathbf{q}) \rangle = \frac{1}{2\pi} \sum_{m,n} \frac{|u_{mn}(q)|^2}{q} \Lambda_{mn}, \quad (2.38)$$

with the *high-gain eigenvalues*

$$\Lambda_{mn} = \sinh^2(G\sqrt{\lambda_{mn}}). \quad (2.39)$$

This expression for the intensity distribution does not depend on the azimuthal angle ϕ (cylindrical symmetry)

and is identical to the one found in Ref. 11 for the Gaussian pump. As was also discussed therein, it is possible to define weights Λ'_{mn} which describe the contribution to the intensity spectrum of each Schmidt mode depending on the gain:

$$\Lambda'_{mn} = \frac{\Lambda_{mn}}{\sum_{m,n} \Lambda_{mn}}. \quad (2.40)$$

The Λ'_{mn} can be understood as the new Schmidt eigenvalues, re-normalized for the high-gain regime¹¹. At low-gain, $G \ll 1$, $\Lambda'_{mn} \approx \lambda_{mn}$.

III. SCHMIDT MODE STRUCTURE

First, we start the analysis by taking a look at the modal structure of the PDC radiation generated from a Laguerre-Gaussian pump beam. To this end, we consider systems of a single BBO crystal and two BBO crystals with an air gap in-between [SU(1,1) interferometer]. Each crystal has a length of $L = 2$ mm and the system is pumped by the Laguerre-Gaussian beam with a width of $w_0 = 50 \mu\text{m}$ and a wavelength of 354.7 nm. For the presented results, we will restrict ourselves to $l_p \geq 0$. However, as is shown in Sec. IV, the results for $l_p < 0$ would not differ qualitatively from the ones presented here. In the following, the intensity profiles are plotted over the external angle $\Theta_s \approx q_s/k_s^{\text{air}}$, where k_s^{air} is the modulus of the wave vector of the signal photons in air. This approximation is valid for small angles withing the paraxial approximation.

In order to determine the connection between the *experimental* gain G_{exp} and the theoretical gain parameter G , we fit^{23,32,33} the collinear output intensity $\langle \hat{N}(0) \rangle d\mathbf{q} d\phi$ of a single crystal with a function of the form $y(\gamma) = B \sinh^2(\tilde{A}\gamma)$, where \tilde{A} and B are the fitting parameters and $G = 2\mathcal{D}\gamma$. The factorization of G is performed to simplify the numerical fitting procedure. Here, \mathcal{D} is a suitable scaling constant; possible choices are for example $\mathcal{D} = 1$ or $\mathcal{D} = 1/C$. The experimental gain G_{exp} is then given by $G_{\text{exp}} = \tilde{A}\gamma = ACG/2$, where the additionally defined constant $A = \tilde{A}/(C\mathcal{D})$ does not depend on the choice of \mathcal{D} . Instead of \tilde{A} , we will only refer to A as the “fit constant” in the following since, once A is known, the theoretical gain parameter G can be calculated given the experimental gain G_{exp} .

In the context of this work, we mainly use the experimental low-gain value of $G_{\text{exp}} = 0.01$ and the high-gain value of $G_{\text{exp}} = 4$, unless specified otherwise. The values for A are listed in Table I. Due to the multimode structure of the PDC radiation, this constant may differ when the fit is performed for the low- or the high-gain regime³², which is why the table lists differing values for A around $G_{\text{exp}} = 0.01$ and $G_{\text{exp}} = 4$.

TABLE I. Fitting parameter A for the selected orbital l_p and radial m_p numbers of the pump.

l_p	m_p	Fitting parameter A	
		$G_{\text{exp}} = 0.01$	$G_{\text{exp}} = 4$
0	0	14.2	17.2
0	7	4.40	9.27
0	18	2.58	5.75
7	0	6.64×10^{-9}	7.22×10^{-9}
7	7	1.99×10^{-7}	2.56×10^{-7}
7	18	1.56×10^{-6}	2.08×10^{-6}
18	0	5.44×10^{-20}	5.87×10^{-20}
18	7	2.03×10^{-17}	2.35×10^{-17}
18	18	1.95×10^{-15}	2.35×10^{-15}

A. Single-crystal setup

For a single crystal, the function g_z containing the spatial integral over the z -axis reads^{10,11}:

$$g_z(q_s, q_i, \phi_s, \phi_i) = L \operatorname{sinc}\left(\frac{L(\mathbf{q}_s - \mathbf{q}_i)^2}{4k_p}\right) e^{iL \frac{(\mathbf{q}_s - \mathbf{q}_i)^2}{4k_p}}, \quad (3.1)$$

where $\operatorname{sinc}(x) = \sin(x)/x$, L is the length of the PDC section, $k_p = |\mathbf{k}_p|$ is the modulus of the pump wave vector and $(\mathbf{q}_s - \mathbf{q}_i)^2 = q_s^2 + q_i^2 - 2q_s q_i \cos(\phi_s - \phi_i)$. Note that here, the Fresnel approximation (paraxial approximation) has been used to express the collinear phase mismatch

$$\Delta k(\mathbf{q}_s, \mathbf{q}_i) = k_{p,z}(\mathbf{q}_s, \mathbf{q}_i) - k_{s,z}(|\mathbf{q}_s|) - k_{i,z}(|\mathbf{q}_i|) \quad (3.2)$$

in an analytically more convenient form by expanding the z -components of the wave vectors to the second order in terms of the transverse wave vectors $|\mathbf{q}_j| \ll |\mathbf{k}_j|$ ^{24,25}:

$$k_{j,z} = \sqrt{|\mathbf{k}_j|^2 - |\mathbf{q}_j|^2} \approx |\mathbf{k}_j| \left(1 - \frac{|\mathbf{q}_j|^2}{2|\mathbf{k}_j|^2}\right), \quad (3.3)$$

where $j = p, s, i$ and $\mathbf{q}_p = \mathbf{q}_s + \mathbf{q}_i$.

Performing the Schmidt decomposition of the Fourier coefficients $\chi_n(q_s, q_i)$ [Eq. (2.19)] of the two-photon amplitude as defined in Eq. (2.4b) with g_{xy} and g_z defined in Eqs. (2.11) and (3.1), respectively, we obtain the normalized eigenvalues λ_{mn} (so that $\sum_{m,n} \lambda_{mn} = 1$). These eigenvalues determine the gain-dependent weights Λ'_{mn} [see Eqs. (2.39) and (2.40)] of the corresponding Schmidt modes and are presented in Fig. 1 for different orbital l_p and radial m_p numbers of the pump. It can be seen that the widths of the distribution in the orbital n and radial m direction become larger with increasing orbital l_p and radial m_p numbers of the pump, respectively [see also Fig. 2(a)]. Therefore, by varying the parameters l_p

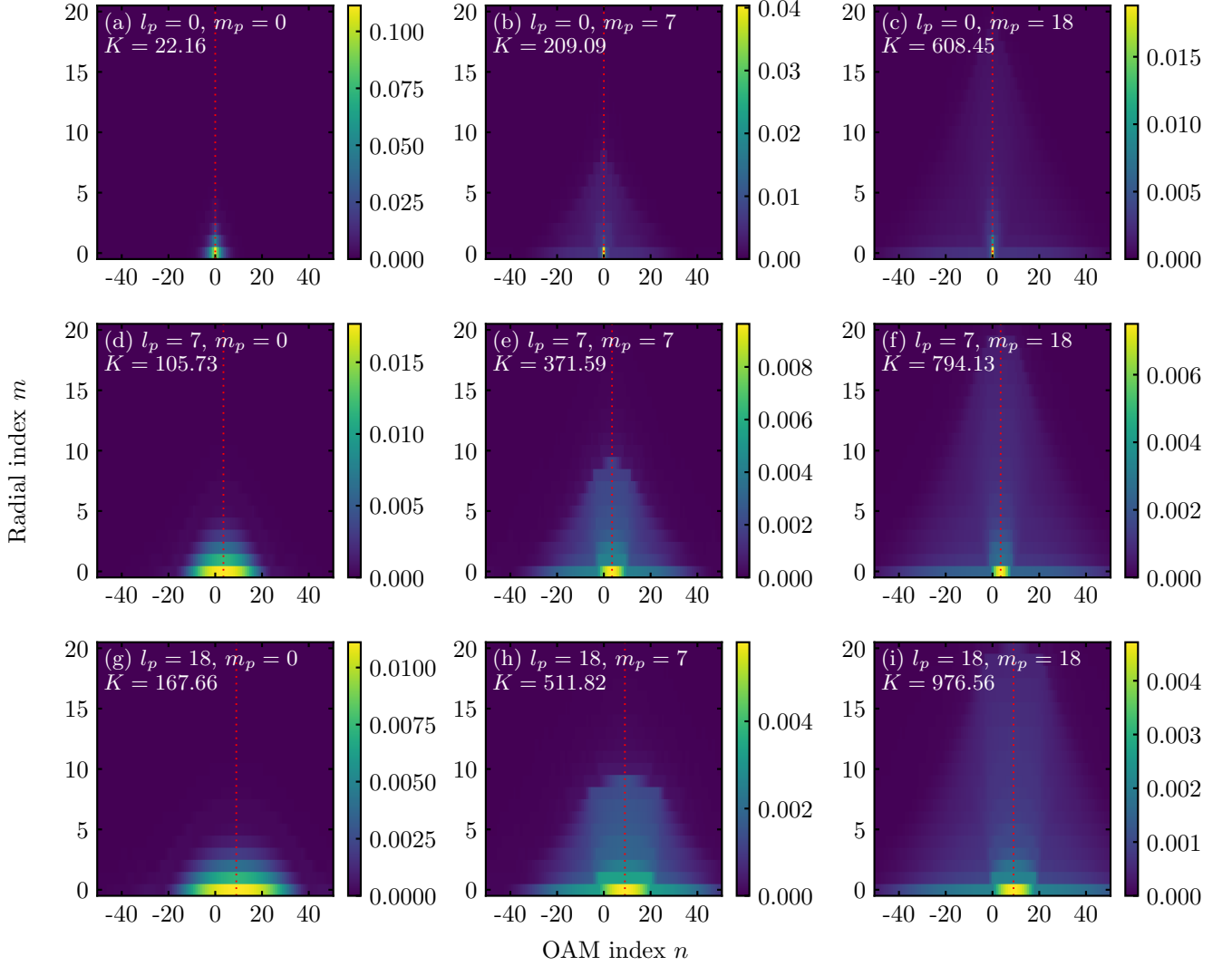


FIG. 1. Normalized modal weights Λ'_{mn} ($\sum_{m,n} \Lambda'_{mn} = 1$) for the low-gain regime ($G = 0.01$), for a single BBO crystal of length $L = 2$ mm pumped by a Laguerre-Gaussian pump with different combinations of orbital l_p and radial m_p indices as mentioned in the plots. The red dotted line indicates the symmetry axis of the eigenvalue distribution at $n = l_p/2$ ($n = 0$, $n = 3.5$ and $n = 9$, for $l_p = 0$, $l_p = 7$ and $l_p = 18$, respectively). The graphs clearly show an increase in the Schmidt number K and the width of the distribution in the radial (along m) and orbital (along n) directions with increasing radial m_p and orbital l_p numbers of the pump, respectively. The width $w_0 = 50$ μm and wavelength 354.7 nm of the pump are fixed for all further plots.

and m_p of the pump beam, one can significantly increase the number of populated OAM and radial modes. To further quantify this, we also provide the Schmidt number (effective mode number)^{11,32}

$$K = \left[\sum_{m,n} (\Lambda'_{mn})^2 \right]^{-1} \quad (3.4)$$

in each 2D plot of eigenvalue distributions. As expected, the Schmidt number increases strongly as l_p and m_p are increased [see Fig. 1].

Furthermore, it is important to point out that the eigenvalue distribution is symmetric with respect to the axis $n = l_p/2$, see Figs. 1, 2(a) and 2(b). This means

that for odd values of l_p , the distribution must be flat around the point $l_p/2$, since the eigenvalues to the left ($n = \lfloor l_p/2 \rfloor$) and to the right ($n = \lceil l_p/2 \rceil$) of this point must be identical, see Fig. 2(a).

For the low-gain regime, the shapes of the intensity spectra for different orbital and radial numbers are shown in Fig. 2(c). They are formed by several Schmidt modes with the weights λ_{mn} according to Eqs. (2.38) and (2.40). For $l_p = 0$ and $m_p = 0$ the intensity distribution has a sinc^2 -shape. The intensity profile becomes more Gaussian with increasing m_p , since the contribution of the fundamental mode (which is Gaussian) becomes higher compared to other modes, see orange curve in Fig. 2(a),

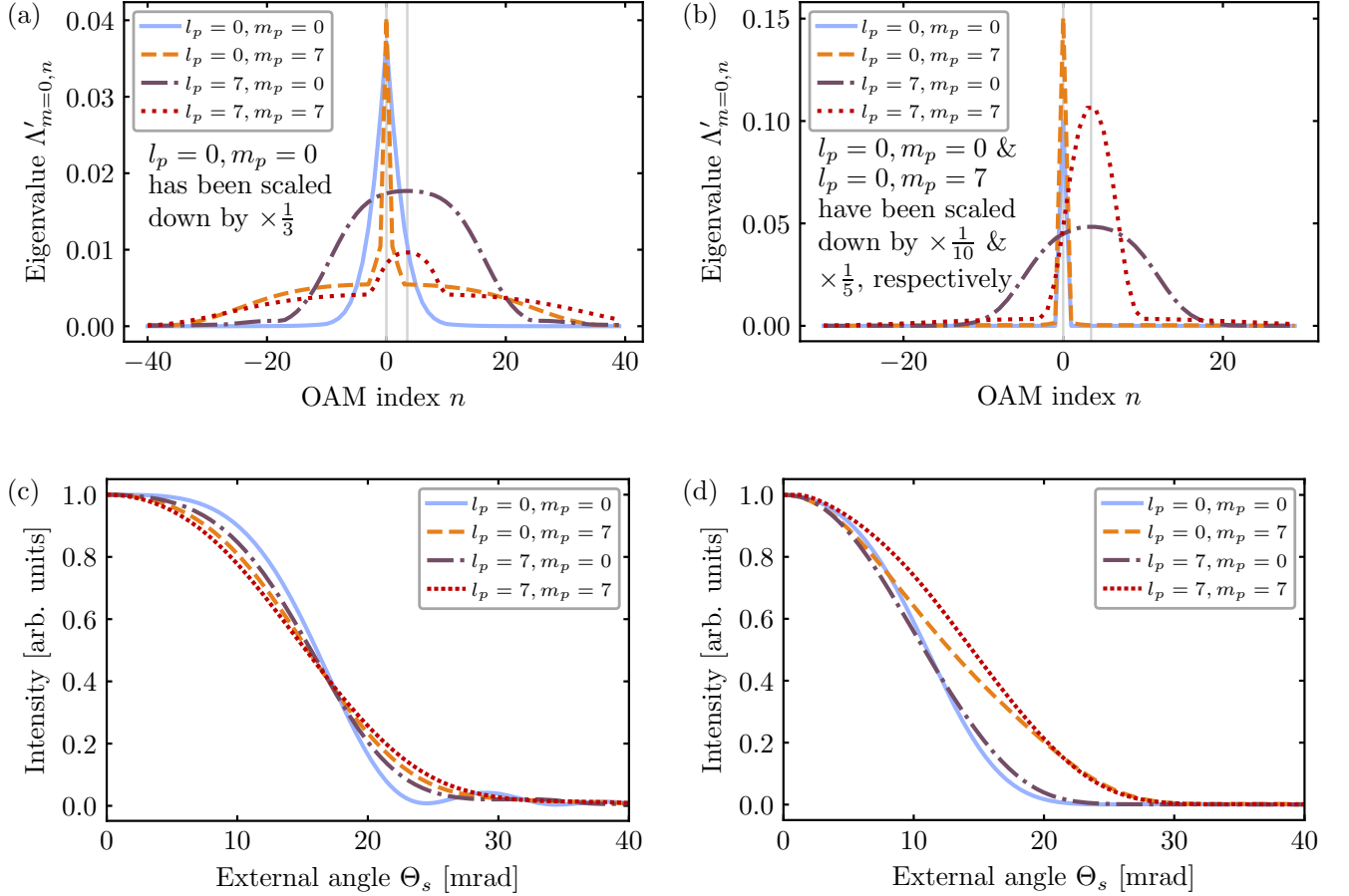


FIG. 2. Cuts of the normalized modal weights $\Lambda'_{m=0,n}$ ($\sum_{m,n} \Lambda'_{mn} = 1$) for the (a) low-gain and (b) high-gain regime for a single BBO crystal of length $L = 2$ mm. The thin gray lines indicate $n = 0$ and $n = 3.5$, which are the symmetry lines for $l_p = 0$ and $l_p = 7$, respectively. The plots (a) and (b) clearly show an increase in the width in the orbital direction (along n) when increasing the radial m_p and orbital l_p numbers of the pump. Normalized intensity spectra for the (c) low-gain and (d) high-gain regime. For $l_p = 0$ and $m_p = 0$ the intensity distribution has a sinc-shape. The intensity profile becomes more Gaussian as l_p and m_p increases.

see also Ref. 11. For nonzero l_p , even though the mode with the largest population is not Gaussian, the number of modes contributing to the total intensity is large enough, so the intensity profile still has a shape which is close to Gaussian.

As we move to the high-gain regime, shown in Fig. 2(b), the eigenvalues are redistributed compared to the low-gain regime¹¹ [see Fig. 2(a)] according to Eq. (2.40) and fewer Schmidt modes contribute to the shape of the intensity spectrum. By reducing the number of contributing modes the eigenvalue distributions and intensity profiles get narrower. Moreover, it can be seen that as l_p and m_p increase, the intensity distribution

becomes wider due to larger mode widths for higher l_p and m_p .

B. Two-crystal setup

An SU(1,1) interferometer consists of two PDC sections with a linear medium in-between. This linear medium imprints a (possibly spatially varying) phase to the pump, signal and idler radiation^{21–23,32}. In this section, we consider a phase which is simply given by the air gap of length d between the two crystals. The function g_z for the two-crystal setup can then be written in the form¹¹:

$$g_z(q_s, q_i, \phi_s, \phi_i) = 2L \operatorname{sinc}\left(L \frac{(q_s - q_i)^2}{4k_p}\right) \cos\left[L \frac{(q_s - q_i)^2}{4k_p} + \frac{\Delta n k_s d}{n_s} + n_s d \frac{(q_s - q_i)^2}{4k_p}\right] \times \exp\left[i\left(L \frac{(q_s - q_i)^2}{2k_p} + \frac{\Delta n k_s d}{n_s} + n_s d \frac{(q_s - q_i)^2}{4k_p}\right)\right], \quad (3.5)$$

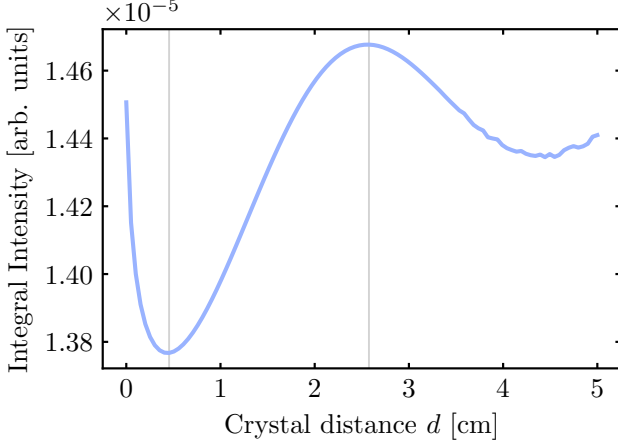


FIG. 3. Integral intensity of the SU(1,1) interferometer output over the distance between the two crystals. The thin gray lines indicate the distances for which the first minimum at $d = 0.42$ cm and the first maximum at $d = 2.52$ cm are observed. Note that the position of the bright and dark fringe seem to be independent of l_p and m_p . To verify this, we compared all 64 combinations of l_p and m_p from 0 to 7 and found that for different l_p and m_p the integral intensities show no significant differences compared to each other and only differ by a scaling factor.

where $\Delta n = n_p^{\text{air}} - \frac{1}{2}(n_s^{\text{air}} + n_i^{\text{air}}) = n_p^{\text{air}} - n_s^{\text{air}}$ and n_j^{air} ($j = p, s, i$) are the refractive indices of the pump, signal and idler radiation in the air gap between the two crystals, while n_s is the refractive index of the signal beam inside the crystal. Here, the Fresnel approximation has again been applied and perfect phase matching is assumed for the collinear direction (where $\mathbf{q}_s = \mathbf{q}_i = \mathbf{0}$), just as in Sec. III A for the single crystal.

Figure 3 presents the integral intensity over the distance d between the crystals that is obtained by integrating the intensity distribution Eq. (2.38) over the radial and azimuthal variables. Here, starting near $d = 3.2$ cm, numerical noise becomes visible. This is caused by the interference in the second crystal which results in peaks in the intensity spectrum that become denser as d increases and are at some point no longer resolved with the chosen numerical grid. Below we will only pay attention to the two special points of this dependence, namely, the first minimum ($d = 0.42$ cm, *dark fringe*) and the first maximum ($d = 2.52$ cm, *bright fringe*), which are shown by the thin gray lines in Fig. 3.

1. Dark fringe

Figure 4 shows the normalized eigenvalue distribution for the first minimum of the total intensity distribution ($d = 0.42$ cm) for different orbital l_p and radial m_p numbers of the pump. It can be seen that the eigenvalue distribution becomes broader and the Schmidt number K is increased for an SU(1,1) interferometer setup compared to the single-crystal setup for the same values of l_p and m_p (compare Figs. 1 and 4).

Furthermore, one can observe that, contrary to the single-crystal configuration, the normalized eigenvalue distributions in the dark-fringe case are characterized by non-monotonic behavior along the orbital direction n . This non-monotonic behavior is observed for nonzero orbital/radial pump numbers and is more clearly visible in the $\lambda_{m=0,n}$ cuts of the modal weight distribution presented in Fig. 5(a). Furthermore, it can be seen that for nonzero orbital pump numbers, the orbital number of the PDC modes with the largest population is no longer $l_p/2$. For example, when $l_p = 7$ and $m_p = 0$, the mode with OAM $n = 11$ has the highest population. In the high-gain regime, a repopulation of the modes takes place¹¹, and the modes with the largest weights are strongly amplified, see Fig. 5(b). This means that in the dark fringe, modes with an OAM higher than the pump OAM can be efficiently populated and filtered at high gain.

These non-trivial eigenvalue profiles result in the non-Gaussian intensity distributions with a complex shape presented in Figs. 5(c) and 5(d) for the low- and high-gain regimes, respectively. Some Schmidt modes which contribute to the intensity distribution are presented in Fig. 16 in Appendix A 1. A high population of modes with high-order OAM in the case of $l_p = 7, m_p = 0$ leads to a donut-shaped intensity profile with a local minimum in the center, which is most pronounced in the high-gain regime.

As already mentioned above, the eigenvalues are symmetrically populated around the point $l_p/2$, due to the fact that $\lambda_{m,l_p-n} = \lambda_{mn}$, see Eq. (2.29a). This means that if modes other than $l_p/2$ are most populated, then there is no single mode that uniquely determines the shape of the intensity distribution in the high-gain regime: There are at least two equally populated modes. By changing the distance between the crystals one can strongly modify the eigenvalue distribution and the OAM of the most populated mode. For example, varying the distance around the dark fringe point, one can change the OAM of the most populated mode from $n = 4$ for

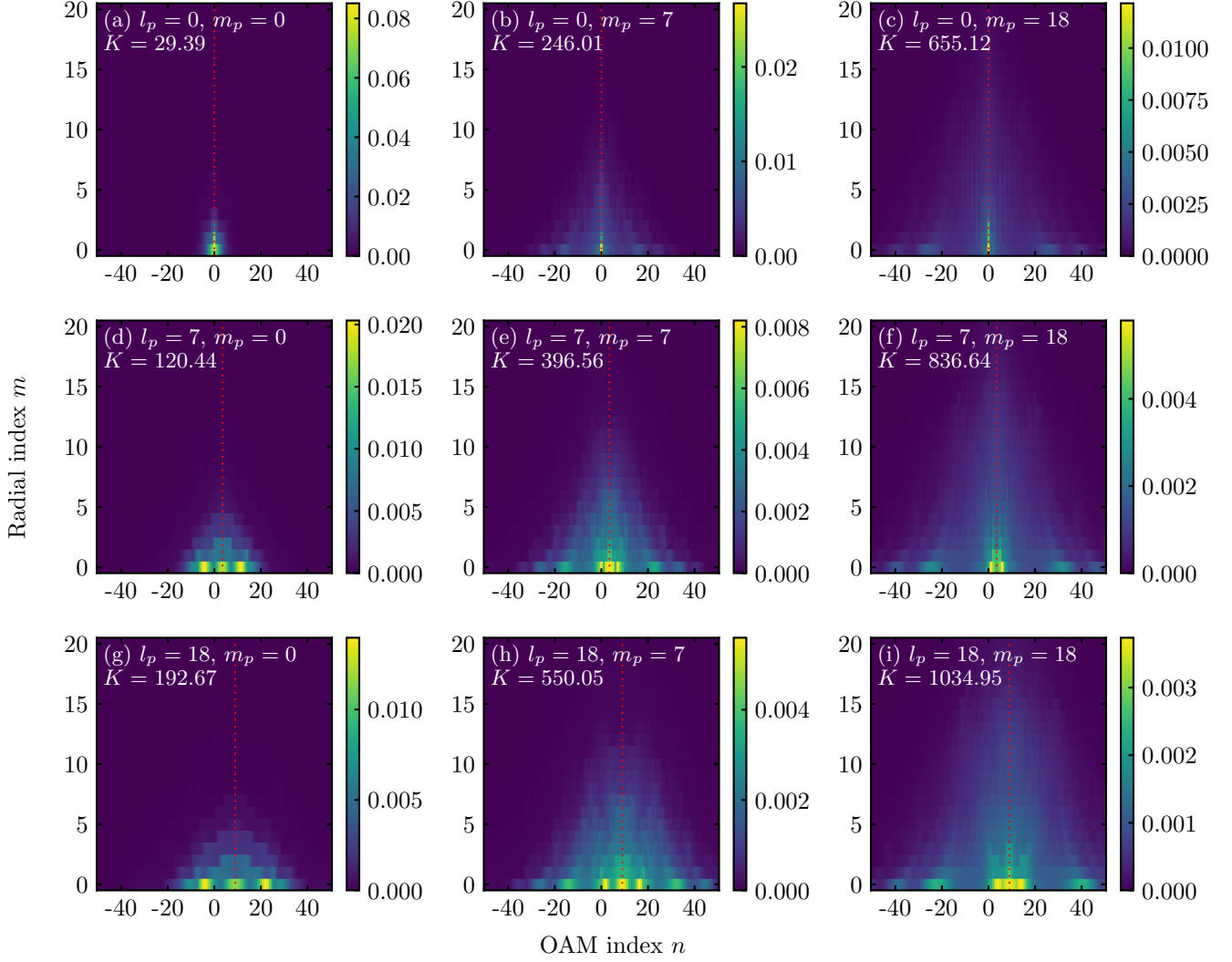


FIG. 4. Normalized modal weight spectra Λ'_{mn} ($\sum_{m,n} \Lambda'_{mn} = 1$) for the low-gain regime ($G = 0.01$), for the two-crystal setup (two BBO crystals, each of length $L = 2$ mm) with an air gap of length $d = 0.42$ cm (dark fringe), pumped by a Laguerre-Gaussian pump with different combinations of orbital l_p and radial m_p indices as written in the plots. The red dotted lines indicate the symmetry axis of the eigenvalue distribution at $n = l_p/2$ ($n = 0, n = 3.5$ and $n = 9$, for $l_p = 0, l_p = 7$ and $l_p = 18$, respectively). The graphs clearly show non-monotonic behavior for the eigenvalue distributions along the orbital direction n and an increase in the Schmidt number compared to the single-crystal case (presented in Fig. 1).

$d = 0.3$ cm to $n = 11$ for $d = 0.42$ cm and $d = 0.5$ cm, see Fig. 6. See also Fig. 17 in Appendix A 2 where the case $l_p = 18$ is discussed.

2. Bright fringe

In the case of the bright fringe ($d = 2.52$ cm), the non-monotonic behavior is less pronounced compared to the dark fringe, see Fig. 7, which shows the normalized eigenvalue distributions for the bright fringe for different orbital l_p and radial m_p numbers of the pump. However, the cuts of the modal weights $\Lambda_{m=0,n}$ presented in Fig. 8 clearly demonstrate that this behavior also occurs here,

while changing in the pump OAM modifies the OAM of the most populated mode [see Fig. 8(a)]. Similarly to the dark fringe, the high-gain regime allows us to filter these most populated modes, see Fig. 8(b).

C. Non-monotonic behavior

As was demonstrated in the previous section, configurations of two crystals with a nonzero distance between the crystals and non-Gaussian pumping can result in a non-monotonic structure of the eigenvalue distribution. This non-monotonic behavior is not observed for a single crystal pumped by a non-Gaussian pump and leads

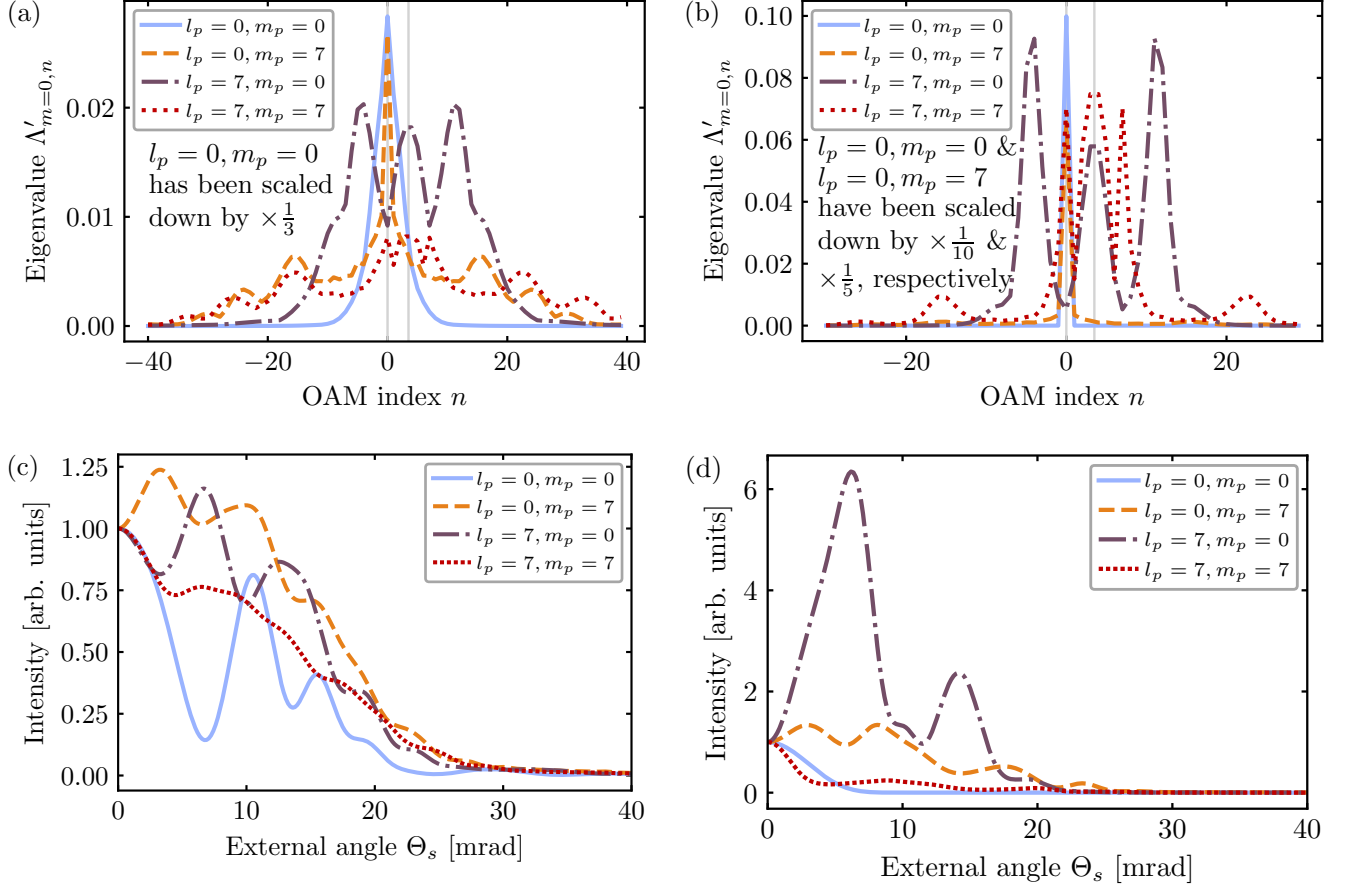


FIG. 5. Cuts of the normalized modal weights $\Lambda'_{m=0,n}$ ($\sum_{m,n} \Lambda'_{mn} = 1$) for the (a) low-gain and (b) high-gain regime for two BBO crystals of length $L = 2$ mm, an air gap between the crystals of length $d = 0.42$ cm (dark fringe) and different orbital l_p and radial m_p numbers of the pump as written in the plots. The thin gray lines indicate $n = 0$ and $n = 3.5$, which are the symmetry lines for $l_p = 0$ and $l_p = 7$, respectively. For a non-Gaussian pump, a non-monotonic behavior in the eigenvalue distribution can be observed. Normalized intensity spectra for the (c) low-gain and (d) high-gain regime. Due to the non-trivial behavior of the eigenvalue distribution, the intensities have a complex non-Gaussian shape at low and high gain.

to configurations where the highest population of modes occurs at an OAM higher than the pump OAM.

To investigate the non-monotonic behavior in more detail, we focus on the *orbital eigenvalues* in the low-gain regime

$$A_n \stackrel{\text{def.}}{=} \sum_m \lambda_{mn}, \quad (3.6)$$

which are the probabilities to find a Schmidt mode with OAM n in the signal/idler field. The orbital eigenvalues can also be obtained by integrating the Fourier coefficients $\chi_n(q_s, q_i)$ introduced in Eq. (2.19), namely,

$$A_n = \iint dq_s dq_i q_s q_i |\chi_n(q_s, q_i)|^2. \quad (3.7)$$

Since the non-monotonic behavior has been observed for any nonzero l_p and any m_p , we set $m_p = 0$ for simplicity, so that the Laguerre polynomials in the pump envelope [Eq. (2.3)] are equal to 1, regardless of the value of l_p . We also define the (complex) constant

$$\bar{A} \stackrel{\text{def.}}{=} 4CL\pi^2 (-1)^{l_p} i^{|l_p|} \left(\frac{w_0}{2}\right)^{|l_p|+1}, \quad (3.8)$$

which includes all prefactors of R that do not depend on q_s , q_i , ϕ_s or ϕ_i [compare Eq. (2.15)].

In order to allow for an analytical treatment, we use the Gaussian approximation $\text{sinc}(b^2 x^2) \approx \exp(-\alpha^2 b^2 x^2)$ for the sinc-function appearing in g_z in Eq. (3.5), where $\alpha = 0.65$ is an additional heuristic scaling factor to achieve a good approximation¹⁰.

The function g_z is then given by

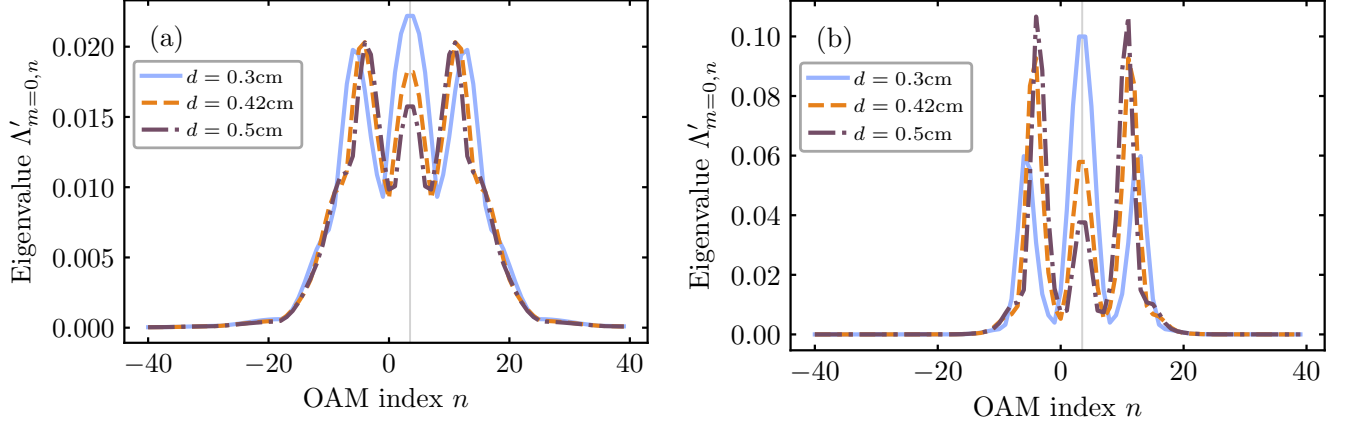


FIG. 6. Cuts of the normalized modal weights $\Lambda'_{m=0,n}$ ($\sum_{m,n} \Lambda'_{mn} = 1$) for $l_p = 7$, $m_p = 0$ for the (a) low-gain and (b) high-gain regime for different distances between the two crystals of an SU(1,1) interferometer around the dark fringe ($d = 0.42$ cm). The thin gray lines indicate $n = l_p/2 = 3.5$. For the distances $d = 0.42$ cm and $d = 0.5$ cm, the most populated OAM mode appears at $n = 11$, which is higher than the pump OAM $l_p = 7$. According to Eq. (2.40), the most populated OAM modes are strongly amplified in the high-gain regime¹¹. See also Fig. 17 in Appendix A 2 which briefly discusses the case $l_p = 18$.

$$g_z(q_s, q_i, \phi_s, \phi_i) = 2L \exp\left(-\alpha^2 L \frac{(q_s - q_i)^2}{4k_p}\right) \cos\left(L \frac{(q_s - q_i)^2}{4k_p} + \frac{\Delta n k_s d}{n_s} + n_s d \frac{(q_s - q_i)^2}{4k_p}\right) \times \exp\left[i\left(L \frac{(q_s - q_i)^2}{2k_p} + \frac{\Delta n k_s d}{n_s} + n_s d \frac{(q_s - q_i)^2}{4k_p}\right)\right]. \quad (3.9)$$

Next, we expand $W(q_s, q_i, \phi_s - \phi_i)$ defined in Eq. (2.13b) using the binomial theorem and abbreviate the angle difference as $\phi_s - \phi_i \stackrel{\text{def.}}{=} \phi$. The Fourier integral from Eq. (2.17) is then given by:

$$\chi_n(q_s, q_i) = \bar{A} \int_0^{2\pi} d\phi \exp\left[-L\alpha^2 \frac{(q_s - q_i)^2}{4k_p} - \left(\frac{w_0 \xi}{2}\right)^2 + i\left(L \frac{(q_s - q_i)^2}{2k_p} + \frac{\Delta n k_s d}{n_s} + n_s d \frac{(q_s - q_i)^2}{4k_p}\right)\right] \times \cos\left(L \frac{(q_s - q_i)^2}{4k_p} + \frac{\Delta n k_s d}{n_s} + n_s d \frac{(q_s - q_i)^2}{4k_p}\right) \sum_{\nu=0}^{l_p} \binom{l_p}{\nu} q_s^\nu q_i^{l_p-\nu} e^{i(n-\nu)\phi}. \quad (3.10)$$

By analytically evaluating the integral over ϕ in the expression above and integrating $|\chi_n(q_s, q_i)|^2$ over q_s and

q_i , one can obtain the orbital eigenvalues Λ_n according to Eq. (3.7):

$$\Lambda_n = A' \int_0^\infty \int_0^\infty dq_s dq_i q_s q_i e^{-a(q_s^2 + q_i^2)} \left| \sum_{\nu=0}^{l_p} \binom{l_p}{\nu} q_s^\nu q_i^{l_p-\nu} \left[e^{i\frac{E}{2}(q_s^2 + q_i^2)} e^{i\mu} J_{n-\nu}(q_s q_i V) + e^{-i\frac{E}{2}(q_s^2 + q_i^2)} e^{-i\mu} J_{n-\nu}(q_s q_i U) \right] \right|^2, \quad (3.11a)$$

where $J_{n-\nu}$ denotes the Bessel functions of order $n - \nu$ and

$$A' = \bar{A}\pi, \quad (3.11b)$$

$$a = \frac{w_0^2}{2} + \frac{L\alpha^2}{2k_p}, \quad (3.11c)$$

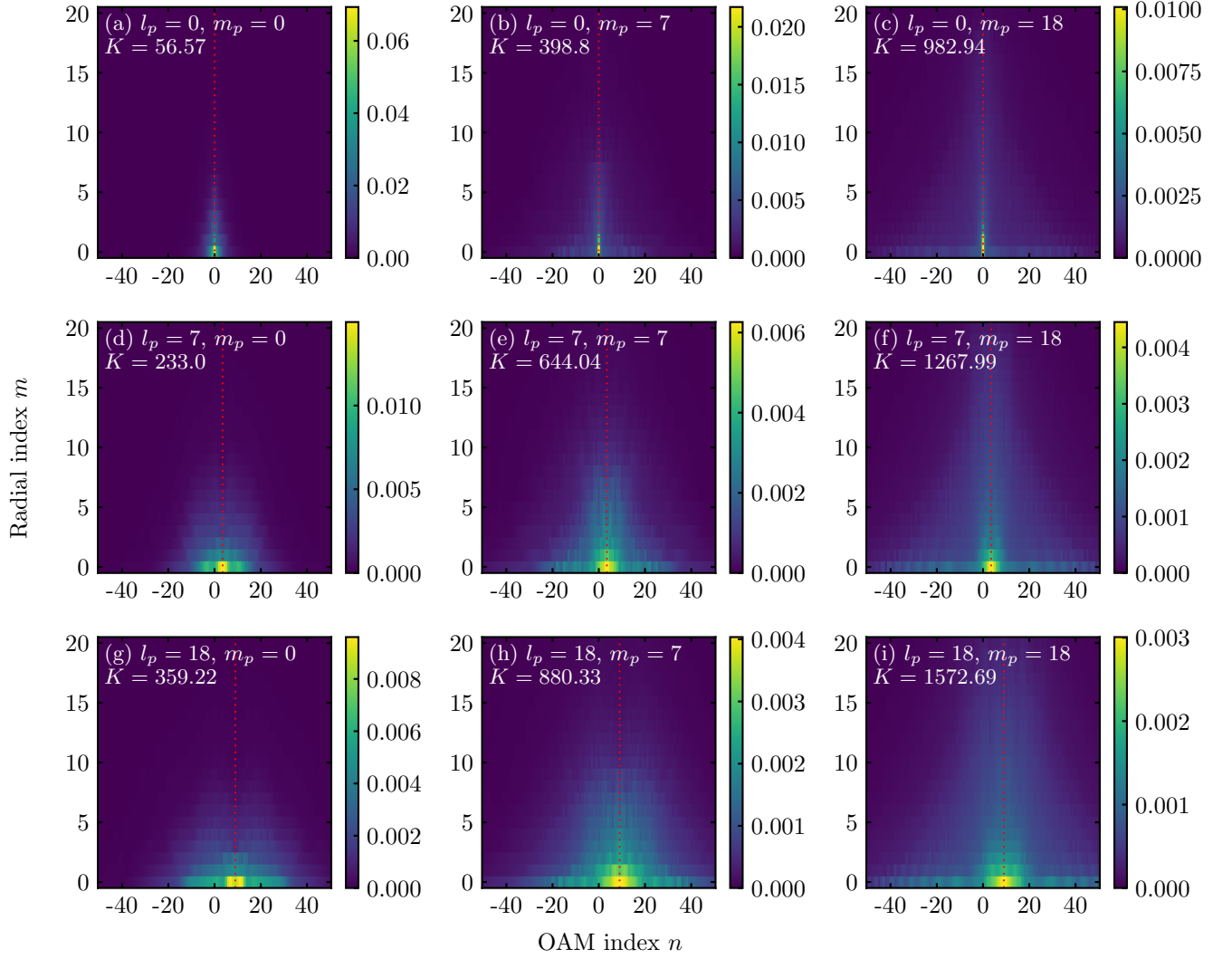


FIG. 7. Normalized modal weight spectra Λ'_{mn} ($\sum_{m,n} \Lambda'_{mn} = 1$) for the low-gain regime ($G = 0.01$), for the two-crystal setup (two BBO crystals, each of length $L = 2$ mm) with an air gap of length $d = 2.52$ cm (bright fringe), pumped by a Laguerre-Gaussian pump with different combinations of orbital l_p and radial m_p indices as written in the plots. The red dotted line indicates the symmetry axis of the eigenvalue distribution at $n = l_p/2$ ($n = 0$, $n = 3.5$ and $n = 9$, for $l_p = 0$, $l_p = 7$ and $l_p = 18$, respectively).

$$E = \frac{L}{2k_p} + \frac{n_s d}{2k_p}, \quad (3.11d)$$

$$\mu = \frac{\Delta n k_s d}{n_s}, \quad (3.11e)$$

$$V = \frac{i w_0^2}{2} - \frac{i L \alpha^2}{2k_p} - \frac{3L}{2k_p} - \frac{n_s d}{k_p}, \quad (3.11f)$$

$$U = \frac{i w_0^2}{2} - \frac{i L \alpha^2}{2k_p} - \frac{L}{2k_p}. \quad (3.11g)$$

From Eq. (3.11a) it can be seen that for $d = 0$, the profile of orbital eigenvalue distribution is defined by a Binomial distribution and the most populated mode has the OAM $n = l_p/2$, while the distribution has a monotonic behavior. However, for $d > 0$, a complicated interfer-

ence takes place (see the term in the brackets) due to the nonzero $\mu = \Delta n k_s d / n_s$ factor. This leads to the suppression of low-order Bessel terms and enhanced contribution of high-order Bessel functions to the eigenvalue distribution, resulting in the non-monotonic behavior. To demonstrate this, we plot the Λ_n obtained from the analytical expression [Eq. (3.11a)] with the Double-Gaussian approximation for different distances between the crystals, see Fig. 9(a) (dashed lines).

It can be seen that a non-monotonic behavior takes place for both constructive and destructive interference points, however, it is more pronounced for the destructive interference configuration. For $d = 0$ the distribution is centred at $n = l_p/2$ and, as predicted, has a monotonic behavior. In the same plot, the numerically calculated or-

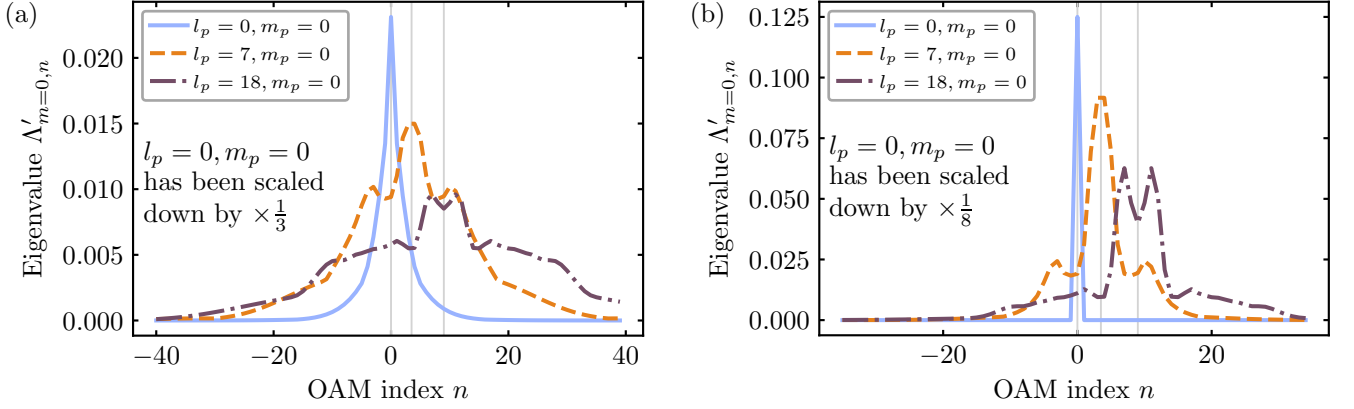


FIG. 8. Cuts of the normalized modal weights $\Lambda'_{m=0,n}$ ($\sum_{m,n} \Lambda'_{mn} = 1$) for the (a) low-gain and (b) high-gain regime for two BBO crystals of length $L = 2$ mm, an air gap of length $d = 2.52$ cm (bright fringe) between the crystals and different orbital l_p and radial m_p numbers of the pump as written in the plots. The thin gray lines indicate $n = 0$, $n = 3.5$ and $n = 9$, which are the symmetry lines for $l_p = 0$, $l_p = 7$ and $l_p = 18$, respectively. Increasing the pump OAM l_p changes the order of the most populated OAM modes.

modal eigenvalues [obtained using g_z with the sinc-term as in Eq. (3.5)] are presented by solid lines. The good agreement between the numerically calculated and analytically evaluated orbital eigenvalues demonstrates the validity of the approximated analytical expression Eq. (3.11a).

The modal weight cuts also demonstrate a qualitative similarity between the two models, see Fig. 9(b), where they are presented for the dark fringe of the interferometer. It is worth noting that in the Double-Gaussian approximation, the point of the dark fringe is shifted, and therefore, the side peaks for the crystal distance $d = 0.42$ cm are not as pronounced as in the case including the sinc-term. However, for the distance $d = 0.55$ cm, we obtain the same picture with more pronounced side peaks compared to the symmetry point $l_p/2$ in the Double-Gaussian approximation.

IV. ANGULAR DISPLACEMENT MEASUREMENT

In this section, we finalize our analysis of PDC with Laguerre-Gaussian pump beams by analyzing the application of the SU(1,1) interferometer for angular displacement detection. As it has already been mentioned in Sec. I, it is possible to use entangled photon states to reach supersensitivity for angular displacement detection^{8,17,18}. In this section, to beat the classical limit, we consider an SU(1,1) interferometer which has a Dove prism placed between the two crystals. A sketch of this setup is presented in Fig. 10.

A Dove prism modifies the electric signal and idler fields in two ways, provided that the fields are not too tightly focused^{18,34}: First, it swaps the helicity of the OAM components of the electric field. For example, if the signal field inside the interferometer (the radiation generated from the first crystal) has an azimuthal de-

pendency $e^{in\phi_s}$ for some $n \in \mathbb{Z}$, then after the prism it is given by $e^{-in\phi_s}$ and, analogously, the helicity is swapped for the idler field. Second, the prism introduces a phase $e^{-in\theta}$ to the field, where θ is the rotation angle of the prism. Note that in our system, this phase is added for both the signal and idler field.

To understand the impact these actions have on the SU(1,1) interferometer, we first analyze the symmetries of the system under a sign change of the pump OAM index. Intuitively, if the sign of l_p is changed, $l_p \rightarrow -l_p$, the results presented in this work should not be affected qualitatively and only change by certain symmetry transformations. To analyze this more rigorously, we add a superscript $[l_p]$ or $[-l_p]$ to the quantities in question, depending on the sign of the pump OAM number.

With this notation, it is immediately clear that for the function W as defined in Eq. (2.13b),

$$W^{[l_p]}(q_s, q_i, \phi_s - \phi_i) = W^{[-l_p]}(q_s, q_i, \phi_i - \phi_s). \quad (4.1)$$

As a consequence, for R as defined in Eq. (2.15), we can see with the help of Eqs. (2.24a) and (2.24b) that

$$R^{[l_p]}(q_s, q_i, \phi_s - \phi_i) = R^{[-l_p]}(q_s, q_i, \phi_i - \phi_s). \quad (4.2)$$

Applying this to the Fourier coefficient integral for χ_n as given in Eq. (2.17) and using the fact that R is 2π -periodic in the angle difference, it can be seen that

$$\chi_n^{[l_p]}(q_s, q_i) = \chi_{-n}^{[-l_p]}(q_s, q_i), \quad (4.3)$$

which therefore also holds for the Schmidt decomposition quantities:

$$\lambda_{mn}^{[l_p]} = \lambda_{m,-n}^{[-l_p]}, \quad (4.4a)$$

$$u_{mn}^{[l_p]} = u_{m,-n}^{[-l_p]}, \quad (4.4b)$$

$$v_{mn}^{[l_p]} = v_{m,-n}^{[-l_p]}. \quad (4.4c)$$

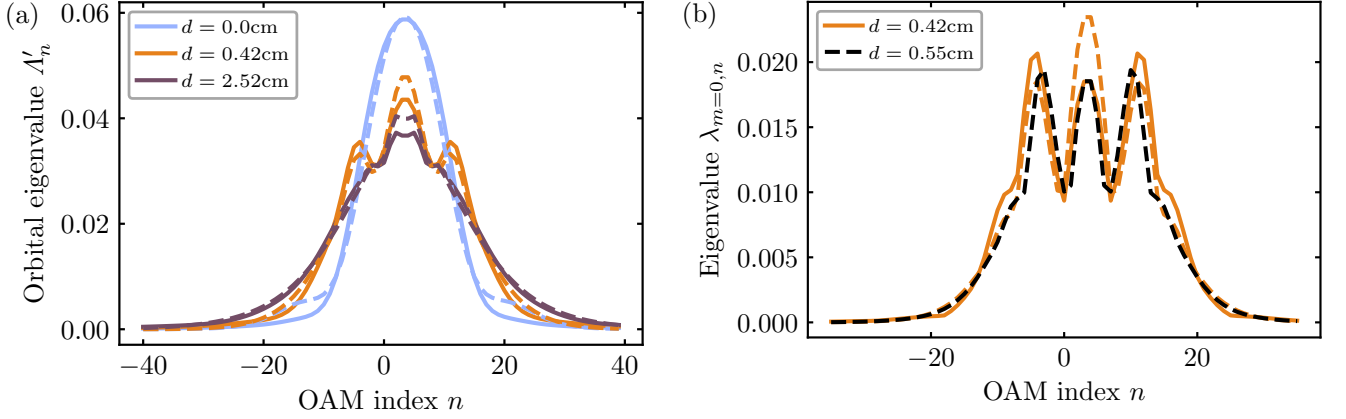


FIG. 9. (a) Normalized orbital eigenvalues $A'_n = A_n / \sum_n A_n$ and (b) cuts of the normalized low-gain modal weights $\lambda_{m=0,n}$ ($\sum_{m,n} \lambda_{mn} = 1$) for different distances d between the two crystals of the SU(1,1) interferometer. Pump parameters are $l_p = 7$ and $m_p = 0$. The curves are calculated using g_z in the form of the sinc-term as in Eq. (3.5) (solid lines) and using the double Gaussian approximation [Eq. (3.11a), dashed lines].

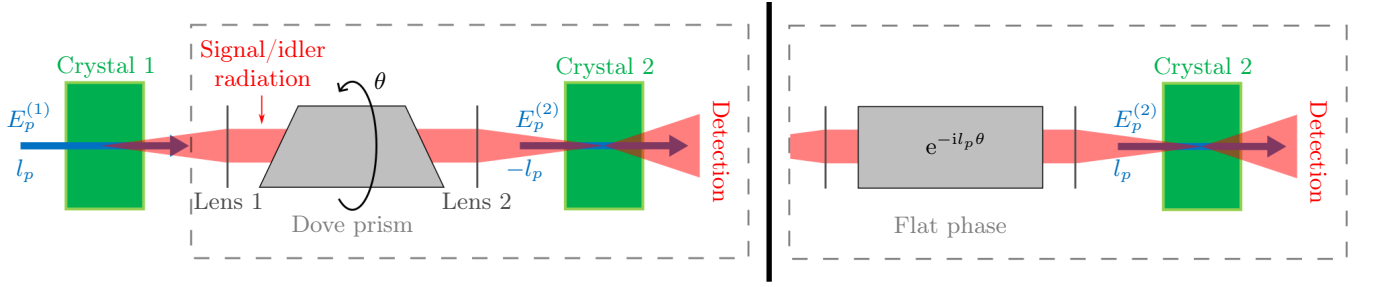


FIG. 10. Left: Sketch of the SU(1,1) interferometer in *diffraction compensated* configuration ($4f$ -lens system)³² with a Dove prism rotated by an angle θ and located between the two lenses in the signal and idler field. The first crystal is pumped by a Laguerre-Gaussian beam $E_p^{(1)}$ with OAM l_p , while the second crystal is pumped by a Laguerre-Gaussian beam $E_p^{(2)}$ with OAM $-l_p$. In an experimental setup, the pump fields can usually be removed after the first crystal and before the detection stage using a dichroic mirror (not shown). Mathematically, the lenses are taken into account via Eq. (4.8)³². Right: Interpretation of the dashed rectangle on the left. As described in the text, the setup shown on the left is mathematically equivalent to instead pumping the second crystal with a Laguerre-Gaussian beam $E_p^{(2)}$ with OAM l_p (same sign as for the first crystal) and adding a flat (constant with respect to \mathbf{q}_p , \mathbf{q}_s and \mathbf{q}_i) phase profile $e^{-il_p\theta}$ to the signal and idler radiation (or, equivalently, to the pump beam), which results in an additional phase factor in the second crystal's TPA, see Eq. (4.7). The structure of the system is then equivalent to the compensated SU(1,1) interferometer considered in Ref. 32, except for the pump shape and the fact that therein, only one transverse dimension is considered. Note that in both the left and right part of the figure, the superscript $(2,D)$ used in the text refers to the subsystem marked with the dashed rectangle.

Therefore, the results for the eigenvalue distributions presented in this work change only in the sense that $n \rightarrow -n$ if the sign of l_p is swapped.

Next, we will derive the TPA describing the Dove prism and the second crystal of the interferometer. In order to differentiate quantities related to each crystal, we will use superscripts (1) and $(2,D)$ for quantities related to the first crystal, and the second crystal including the Dove prism,

respectively. Note that the latter superscript refers to the subsystem marked with the dashed rectangle in Fig. 10.

Assuming that the second crystal is pumped with a Laguerre-Gaussian beam with OAM quantum number $-l_p$, the Fourier decomposition of its TPA $F^{(2,D),[-l_p]}$ [compare Eq. (2.18)] can be written in the following form, taking into account the additional phase factors and sign changes due to the Dove prism as described above:

$$F^{(2,D),[-l_p]}(q_s, q_i, \phi_s, \phi_i) = \frac{1}{2\pi} \sum_n \chi_n^{(2),[-l_p]}(q_s, q_i) e^{in\phi_s} e^{in\theta} e^{i(-l_p-n)\phi_i} e^{i(-l_p-n)\theta}. \quad (4.5)$$

Note that χ_n , which for each n only contains information regarding the radial parts of the Schmidt modes, is not affected by the Dove prism and therefore only has a superscript ⁽²⁾. After using $n + (-l_p - n) = -l_p$ and flipping the sign of the summation index $n \rightarrow -n$, the equation above can be written as

$$F^{(2,D),[-l_p]}(q_s, q_i, \phi_s, \phi_i) = \frac{e^{-il_p\theta}}{2\pi} \sum_n \chi_n^{(2),[l_p]}(q_s, q_i) e^{-in\phi_s} e^{-i(l_p-n)\phi_i}, \quad (4.6)$$

where Eq. (4.3) has been used to rewrite $\chi_{-n}^{(2),[-l_p]}(q_s, q_i) = \chi_n^{(2),[l_p]}(q_s, q_i)$. Clearly, the right-hand side of Eq. (4.6) represents the decomposition of the TPA that corresponds to the second crystal without a prism, pumped by a beam with an OAM l_p and multiplied with an additional phase factor $e^{-il_p\theta}$:

$$F^{(2,D),[-l_p]}(\mathbf{q}_s, \mathbf{q}_i) = e^{-il_p\theta} F^{(2),[l_p]}(\mathbf{q}_s, \mathbf{q}_i). \quad (4.7)$$

This expression provides an alternative way to understand how the Dove prism affects the interferometer: Placing the Dove prism in the signal and idler radiation arm is effectively equivalent to pumping the second crystal of an interferometer without the Dove prism with the OAM of opposite helicity and adding an extra phase factor $e^{-il_p\theta}$ to the TPA of the second crystal. This interpretation of the setup is shown on the right hand side in Fig. 10.

Furthermore, note that in the *diffraction compensated* SU(1,1) interferometer configuration³² (“wide-field SU(1,1) interferometer”²²) the TPAs of the first and second crystal are related via

$$F^{(2),[l_p]}(\mathbf{q}_s, \mathbf{q}_i) = F^{(1),[l_p]}(\mathbf{q}_s, \mathbf{q}_i), \quad (4.8)$$

which can be seen by applying the results of Sec. II of Ref. 32 to the function g_z for the second crystal: For the non-compensated case, this function is described by the integral

$$g_z^{(2)}(\mathbf{q}_s, \mathbf{q}_i) = \int_L^{2L} dz e^{i\Delta k z}, \quad (4.9)$$

while for the compensated setup, this function is instead given by⁴

$$g_z^{(2)}(\mathbf{q}_s, \mathbf{q}_i) = \int_L^{2L} dz e^{-i\Delta k[z-2L]} = \int_0^L dz e^{i\Delta k z}, \quad (4.10)$$

which is identical to the integral for the first crystal. Hence, in this configuration, the TPA of the second crystal can ultimately be written as:

$$F^{(2,D),[-l_p]}(\mathbf{q}_s, \mathbf{q}_i) = F^{(1),[l_p]}(\mathbf{q}_s, \mathbf{q}_i) e^{-il_p\theta}. \quad (4.11)$$

Using this relationship, in the following, we will express all quantities via the quantities of the first crystal. Furthermore, for readability, we will omit the $[\pm l_p]$ superscripts below.

One way of connecting the TPAs of the first and the second crystal including the Dove prism is by using the fact that the output plane-wave operators of the first crystal must coincide with the input plane-wave operators of the subsystem consisting of the Dove prism and the second crystal. This approach has previously been used for the description of SU(1,1) interferometers in Ref. 32.

To implement this approach for the angular displacement measurements, we first bring Eq. (2.37) into the form

$$\begin{aligned} \hat{a}^{\text{out}}(\mathbf{q}) &= \int d^2q' \tilde{\eta}(\mathbf{q}, \mathbf{q}') \hat{a}^{\text{in}}(\mathbf{q}') \\ &\quad + \int d^2q' \beta(\mathbf{q}, \mathbf{q}') [\hat{a}^{\text{in}}(\mathbf{q}')]^\dagger \end{aligned} \quad (4.12)$$

and find that the *transfer functions* $\tilde{\eta}$ and β connecting the input and output plane-wave operators are given by

⁴ The apparent difference of the first integrand in Eq. (4.10) to the function defined in Eq. (2.9) of Ref. 32 comes from the fact that therein, the z -axis integration for the second crystal is taken over the interval $[0, L]$ (reflection geometry) instead of $[L, 2L]$ (transmission geometry), as in the current paper.

$$\tilde{\eta}(\mathbf{q}, \mathbf{q}') = \frac{1}{2\pi} \sum_{m,n} \sqrt{\tilde{\Lambda}_{mn}} \frac{u_{mn}(q)}{\sqrt{q}} \frac{u_{mn}^*(q')}{\sqrt{q'}} e^{-in(\phi - \phi')}, \quad (4.13a)$$

$$\beta(\mathbf{q}, \mathbf{q}') = \frac{1}{2\pi} \sum_{m,n} \sqrt{\Lambda_{mn}} \frac{u_{mn}(q)}{\sqrt{q}} \frac{v_{mn}(q')}{\sqrt{q'}} e^{-in\phi} e^{-i(l_p - n)\phi'}, \quad (4.13b)$$

where Λ_{mn} is defined as in Eq. (2.39) and where

$$\tilde{\Lambda}_{mn} = \cosh^2 \left(G \sqrt{\lambda_{mn}} \right). \quad (4.14)$$

Note that the expression for β is similar to the TPA F as given in Eq. (2.21), except for the fact that the singular values $\sqrt{\lambda_{mn}}$ are replaced with the square roots of the high-gain eigenvalues $\sqrt{\Lambda_{mn}}$.

In this formalism, each subsystem (the first crystal and the second crystal with the Dove prism) has its own set of transfer functions which we will mark with the corresponding superscripts as introduced above. The transfer functions connecting the input and output operators of the entire interferometer are then given by³²:

$$\begin{aligned} \tilde{\eta}^{(\text{SU})}(\mathbf{q}, \mathbf{q}') &= \int d^2 \bar{q} \tilde{\eta}^{(2,D)}(\mathbf{q}, \bar{\mathbf{q}}) \tilde{\eta}^{(1)}(\bar{\mathbf{q}}, \mathbf{q}') \\ &\quad + \int d^2 \bar{q} \tilde{\eta}^{(2,D)}(\mathbf{q}, \bar{\mathbf{q}}) \left[\beta^{(1)}(\bar{\mathbf{q}}, \mathbf{q}') \right]^*, \end{aligned} \quad (4.15a)$$

$$\begin{aligned} \beta^{(\text{SU})}(\mathbf{q}, \mathbf{q}') &= \int d^2 \bar{q} \tilde{\eta}^{(2,D)}(\mathbf{q}, \bar{\mathbf{q}}) \beta^{(1)}(\bar{\mathbf{q}}, \mathbf{q}') \\ &\quad + \int d^2 \bar{q} \tilde{\eta}^{(2,D)}(\mathbf{q}, \bar{\mathbf{q}}) \left[\tilde{\eta}^{(1)}(\bar{\mathbf{q}}, \mathbf{q}') \right]^*. \end{aligned} \quad (4.15b)$$

For both subsystems, the transfer functions can be obtained by applying the decomposition of the corresponding TPA to their definitions Eqs. (4.13a) and (4.13b).

Furthermore, note that since the additional phase factor $e^{-il_p\theta}$ in Eq. (4.11) does not depend on \mathbf{q}_s or \mathbf{q}_i , one can find a direct connection between the Schmidt modes and the eigenvalues of both subsystems:

$$u_{mn}^{(1)}(q) e^{-i\frac{l_p}{2}\theta} = u_{mn}^{(2,D)}(q), \quad (4.16a)$$

$$v_{mn}^{(1)}(q) e^{-i\frac{l_p}{2}\theta} = v_{mn}^{(2,D)}(q), \quad (4.16b)$$

$$\lambda_{mn}^{(1)} = \lambda_{mn}^{(2,D)}. \quad (4.16c)$$

Substituting this to Eqs. (4.13a) and (4.13b), it becomes immediately clear that the transfer functions of both subsystems are connected via

$$\tilde{\eta}^{(2,D)}(\mathbf{q}, \mathbf{q}') = \tilde{\eta}^{(1)}(\mathbf{q}, \mathbf{q}'), \quad (4.17a)$$

$$\beta^{(2,D)}(\mathbf{q}, \mathbf{q}') = \beta^{(1)}(\mathbf{q}, \mathbf{q}') e^{-il_p\theta}. \quad (4.17b)$$

These expressions are analogous⁵ to Eqs. (4.1a) and (4.1b) of Ref. 32 and greatly simplify the following steps. For example, using Eq. (4.15b) and the properties of the eigenvalues given in Eqs. (2.29a)–(2.29c), it can be shown that the high-gain eigenvalues of the entire interferometer are given by

$$\Lambda_{mn}^{(\text{SU})} = 4\Lambda_{mn}^{(1)} \left(\Lambda_{mn}^{(1)} + 1 \right) \cos^2 \left(\frac{l_p}{2} \theta \right). \quad (4.18)$$

The sensitivity for the measurement of the rotation angle θ of the Dove prism can be obtained from the error propagation relation in terms of the integral output intensity $\langle \hat{N}_{\text{tot}} \rangle = \int d^2 q \langle \hat{N}_s(\mathbf{q}) + \hat{N}_i(\mathbf{q}) \rangle = 2 \int d^2 q \langle \hat{N}_s(\mathbf{q}) \rangle$ and output covariance function $\text{cov}(\mathbf{q}_s, \mathbf{q}_i)$ of the interferometer^{18,32}:

$$\Delta\theta = \frac{\langle \Delta \hat{N}_{\text{tot}} \rangle}{\left| \frac{d\langle \hat{N}_{\text{tot}} \rangle}{d\theta} \right|} = \frac{\sqrt{\iint d^2 q_s d^2 q_i \text{cov}(\mathbf{q}_s, \mathbf{q}_i)}}{\left| \frac{d\langle \hat{N}_{\text{tot}} \rangle}{d\theta} \right|}. \quad (4.19)$$

Note that this expression is identical to the definition of the phase sensitivity in SU(1,1) interferometers. Therefore, the angular sensitivity for the interferometer can be rewritten by using Eqs. (2.39), (4.12)–(4.14), (4.17a) and (4.17b) and following the necessary steps as in Sec. IV of Ref. 32:

$$\Delta\theta_{\text{TF}} = \frac{\sqrt{2}}{2} \frac{\sqrt{\mathcal{A} + 4\mathcal{B} \cos^2 \left(\frac{l_p}{2} \theta \right)}}{\mathcal{A} |l_p| \left| \sin \left(\frac{l_p}{2} \theta \right) \right|}, \quad (4.20a)$$

with

$$\mathcal{A} = \sum_{mn} \Lambda_{mn}^{(1)} \left(\Lambda_{mn}^{(1)} + 1 \right), \quad (4.20b)$$

$$\mathcal{B} = \sum_{mn} \left[\Lambda_{mn}^{(1)} \left(\Lambda_{mn}^{(1)} + 1 \right) \right]^2, \quad (4.20c)$$

where we have added the subscript _{TF} to $\Delta\theta$ to indicate that it was obtained by connecting the two subsystems

⁵ In Ref. 32 these relationships were derived directly from the integro-differential equations describing the evolution of the plane-wave operators. Note that from Eq. (4.13a) it follows that $\tilde{\eta}(\mathbf{q}, \mathbf{q}') = [\tilde{\eta}(\mathbf{q}', \mathbf{q})]^*$. However, it should be emphasized that this does not hold at high-gain when time ordering effects are included^{23,32}.

using the transfer functions. The additional factor $\sqrt{2}$ results from the fact that we consider indistinguishable signal and idler photons, see Sec. IID.

Clearly, the above expression for $\Delta\theta_{\text{TF}}$ diverges for $l_p = 0$. In this case, the pump beam is a Gaussian for $m_p = 0$ and circularly symmetric for any m_p . Since there is no preferred transverse direction in the system, the combined signal-idler field must also be circularly symmetric. This can be seen from the fact that for $l_p = 0$, the TPA only depends on the signal-idler angle difference $\phi_s - \phi_i$, but not on the absolute values of the angles, see Eq. (2.21) and Ref. 11. Due to this symmetry, the Dove prism does not modify the signal-idler field generated by the first crystal in a detectable manner and it is therefore not possible to detect the rotation angle of the Dove prism for $l_p = 0$.

Alternatively to the *transfer-function approach* presented above, there is a purely Schmidt-mode theory based approach to obtain an expression for $\Delta\theta$. In this case, the TPA $F^{(\text{SU})}$ for the SU(1,1) interferometer can be written as

$$F^{(\text{SU})}(\mathbf{q}_s, \mathbf{q}_i) = F^{(1)}(\mathbf{q}_s, \mathbf{q}_i) + F^{(2,D)}(\mathbf{q}_s, \mathbf{q}_i). \quad (4.21)$$

This is analogous to the way the TPA is calculated for the SU(1,1) interferometers and results in g_z as given in Eqs. (3.5) and (3.9).

An alternative way to obtain this result can be seen from Eqs. (2.39) and (4.13a)–(4.14) as follows: For $G \ll 1$, $\sinh(G\sqrt{\lambda_{mn}}) \approx G\sqrt{\lambda_{mn}}$ and $\cosh(G\sqrt{\lambda_{mn}}) \approx 1$, meaning

$$\tilde{\eta}(\mathbf{q}, \mathbf{q}') \approx \delta^{(2)}(\mathbf{q} - \mathbf{q}'), \quad (4.22a)$$

$$\beta(\mathbf{q}, \mathbf{q}') \approx G F(\mathbf{q}, \mathbf{q}'), \quad (4.22b)$$

where $\delta^{(2)}$ is the two-dimensional Dirac delta function. With these two expressions for the transfer functions, Eq. (4.15b) simplifies to Eq. (4.21). Note that there is no distinction between whether \mathbf{q} and \mathbf{q}' correspond to \mathbf{q}_s or \mathbf{q}_i due to the degeneracy, see Sec. IID.

Next, applying the connection between the TPAs for the two subsystems given in Eq. (4.11) to Eq. (4.21) yields:

$$F^{(\text{SU})}(\mathbf{q}_s, \mathbf{q}_i) = F^{(1)}(\mathbf{q}_s, \mathbf{q}_i) (1 + e^{-il_p\theta}). \quad (4.23)$$

This connection between the TPA of the interferometer and the first crystal allows us to define the eigenvalues of the Schmidt decomposition of the interferometer as

$$\lambda_{mn}^{(\text{SU})} = 4\lambda_{mn}^{(1)} \cos^2\left(\frac{l_p}{2}\theta\right), \quad (4.24)$$

since, as mentioned above, the rotation angle θ does not depend on the transverse wave-vector components \mathbf{q}_s and \mathbf{q}_i . From there, the high-gain eigenvalues follow as

$$\Lambda_{mn}^{(\text{SU})} = \sinh^2\left[2G\sqrt{\lambda_{mn}} \cos\left(\frac{l_p}{2}\theta\right)\right]. \quad (4.25)$$

Note that this expression is not exactly equivalent to the *transfer function* case considered above, compare Eq. (4.18). However, for $G \ll 1$, Eqs. (4.18) and (4.25) coincide.

Using Eq. (4.25), one can evaluate the expression for $\Delta\theta$ given by Eq. (4.19) as follows:

$$\Delta\theta_{\text{SMT}} = \frac{\sqrt{2}}{2} \frac{1}{G |l_p| \left| \sin\left(\frac{l_p}{2}\theta\right) \right|} \frac{\sqrt{\sum_{mn} \sinh^2\left[4G\sqrt{\lambda_{mn}} \cos\left(\frac{l_p}{2}\theta\right)\right]}}{\sum_{mn} \sqrt{\lambda_{mn}} \sinh\left[4G\sqrt{\lambda_{mn}} \left| \cos\left(\frac{l_p}{2}\theta\right) \right| \right]}, \quad (4.26)$$

where we have added the subscript SMT to indicate that this expression was obtained by using the Schmidt-mode theory, instead of the transfer functions as in Eq. (4.20a). Note that this expression is, in general, not equal to $\Delta\theta_{\text{TF}}$ as defined in Eq. (4.20a). However, for low-gain $G \ll 1$, both of these expressions coincide:

$$\Delta\theta_{G \ll 1} \approx \frac{\sqrt{2}}{2} \frac{1}{G |l_p| \left| \sin\left(\frac{l_p}{2}\theta\right) \right|}. \quad (4.27)$$

Clearly, the differences in Δ_{TF} and Δ_{SMT} must be related to the fact of how we introduce the displacement phase: In the transfer functions approach, both crystals are treated separately and the angular displacement phase

is applied to the solution for the operators of the second crystal, thereby introducing ordering in time, which is not the case for the Schmidt-mode theory approach where both TPAs are directly added together [see Eq. (4.21)].

Usually, the sensitivity $\Delta\theta$ is normalized with respect to the classical limit, that is, the shot noise level (SNL, the standard quantum limit¹⁸), which is defined by

$$\Delta\theta_{\text{SNL}} = \frac{1}{\sqrt{\langle \hat{N}_{\text{tot}}^{(1)} \rangle}}, \quad (4.28)$$

where $\langle \hat{N}_{\text{tot}}^{(1)} \rangle$ is the total intensity inside the interferometer that interacts with the Dove prism, that is, the total

intensity of the signal and idler radiation generated by the first crystal: $\langle \hat{N}_{\text{tot}}^{(1)} \rangle = 2\langle \hat{N}_{s,\text{tot}}^{(1)} \rangle = 2 \int d^2q \langle \hat{N}_s^{(1)}(\mathbf{q}) \rangle$. Then, the normalized angular displacement sensitivity reads

$$f = \frac{\Delta\theta}{\Delta\theta_{\text{SNL}}} \quad (4.29)$$

and can be evaluated using either the transfer functions approach [Eqs. (4.20a)–(4.20c)] or the Schmidt-mode theory [Eq. (4.26)].

The results for f as a function of the rotation angle θ for both approaches are presented in Fig. 11. Note that, for simplicity, we average the values for the fitting constant A for the low- and high-gain regime and use only the average value in this section. This is justified by the experimental technique for measuring this constant, in which the relatively large measurement error exceeds the difference between the constants for the low and high-gain regime³³. Furthermore, this approximation will greatly simplify the following steps, where we consider ranges of G_{exp} values.

Here, Fig. 11(d) shows that, in the low-gain regime, the angular sensitivity does not depend on the radial pump number m_p , which is consistent with Eq. (4.27). As the gain increases, according to the rigorous transfer functions approach, the angular sensitivity improves for all orbital numbers of the pump, see Figs. 11(a)–11(c). In all cases, f is $2\pi/l_p$ -periodic, which is expected from the analytic expressions of $\Delta\theta$ [see Eqs. (4.20a)–(4.20c) and also Eq. (4.26)]. At the same time, the role of the radial pump number becomes visible: The angular sensitivity improves with increasing radial pump number when both the gain and the orbital pump number are fixed. However, in the high-gain regime, the angular sensitivity calculated using the Schmidt-mode approach (where the angular displacement is included directly in the TPA for the interferometer) differs from the prediction of the transfer functions approach due to the fact that the ordering in time in regard to the applied angular displacement phase is not accounted for, which restricts the applicability of the Schmidt-mode approach.

Evidently, for $\theta \rightarrow 2\pi n/l_p$, $n \in \mathbb{Z}$, both Δ_{TF} and Δ_{SMT} diverge regardless of G , see Eq. (4.20a) and Eq. (4.26). Furthermore, $\Delta\theta_{\text{TF}}$ in Eq. (4.20a) is minimized for any $\theta = \pi(2n+1)/l_p$, $n \in \mathbb{Z}$, which is confirmed by the plots in Fig. 11. Since the SNL does not depend on θ , the optimal (minimal) SNL-normalized angular sensitivity f is also achieved at the aforementioned values for θ and is given by

$$f_{\text{TF,min}} = \frac{1}{|l_p|} \sqrt{\frac{\langle \hat{N}_{s,\text{tot}}^{(1)} \rangle}{\mathcal{A}}}. \quad (4.30)$$

The optimal (minimal) SNL-normalized sensitivity for the transfer function approach $f_{\text{TF,min}}$ as a function of the experimental gain G_{exp} is shown in Fig. 12 for selected values of l_p and m_p . Clearly, the optimal SNL-normalized angular sensitivity improves strongly with in-

creasing the gain. For low-gain, the quadratic contribution $\sum_{m,n} (\Lambda_{mn}^{(1)})^2$ in \mathcal{A} [see Eq. (4.20b)] becomes negligible and $f_{\text{TF,min}}$ behaves as:

$$\lim_{G_{\text{exp}} \searrow 0} f_{\text{TF,min}} = \frac{1}{|l_p|}. \quad (4.31)$$

Indeed, in the low-gain regime, the shown normalized angular sensitivity does not depend on the pump radial number, see Fig. 12.

Furthermore, we may rewrite Eq. (4.30) in terms of the number of effective modes³²:

$$f_{\text{TF,min}} = \frac{1}{|l_p|} \frac{1}{\sqrt{1 + \frac{\langle \hat{N}_{s,\text{tot}}^{(1)} \rangle}{K^{(1)}}}}, \quad (4.32)$$

with the Schmidt number (effective mode number) $K^{(1)}$ as defined in Eq. (3.4), which is here defined using the normalized first crystal eigenvalues $\Lambda_{mn}^{(1)}$ [see Eq. (2.40)].

The behavior of the optimal angular sensitivity for the transfer function approach in the multimode regime is similar to the behavior of the optimal phase sensitivity discussed in Ref. 32: The angular sensitivity can be improved by increasing the intensity inside the interferometer and reducing the effective mode number. Interestingly, a reduction of both the number of OAM and radial modes leads to an improvement in the sensitivity.

Moreover, in the high-gain regime, the radial pump number strongly affects the angular sensitivity: The higher the radial pump number is, the better the angular sensitivity becomes at high gain for the selected pump OAM values, see Fig. 12. This might seem counterintuitive at first, since increasing m_p increases the Schmidt number $K^{(1)}$ as discussed in Sec. III A. However, with increasing gain, the number of effective modes is reduced since the most populated modes are amplified more strongly¹¹. This behavior is confirmed by the plots of the Schmidt numbers as a function of the experimental gain shown in Fig. 13.

Similarly to Refs. 17 and 18, we find a prefactor $1/|l_p|$ for the optimal sensitivity [Eq. (4.30)]. However, since the integral intensity $\langle \hat{N}_{s,\text{tot}}^{(1)} \rangle$, the factor \mathcal{A} and the fitting constant A relating the experimental and theoretical gain also depend on l_p , it is not clear that the optimal sensitivity overall scales as $1/|l_p|$. Indeed, since we focus on multimode PDC radiation, the behavior of f_{TF} and $f_{\text{TF,min}}$ as a function of l_p is less obvious. Nevertheless, as shown above in Eq. (4.31), this behavior is recovered exactly as $f_{\text{TF,min}} = 1/|l_p|$ in the low-gain limit and surpasses this value for high gain for the selected values of l_p and m_p , see Fig. 12.

For experimental applications, the width of the angular supersensitivity region Δ is an important parameter since it must be large enough to allow for stable measurements. By setting $f_{\text{TF}}(\theta) \stackrel{!}{=} 1$, one can obtain the

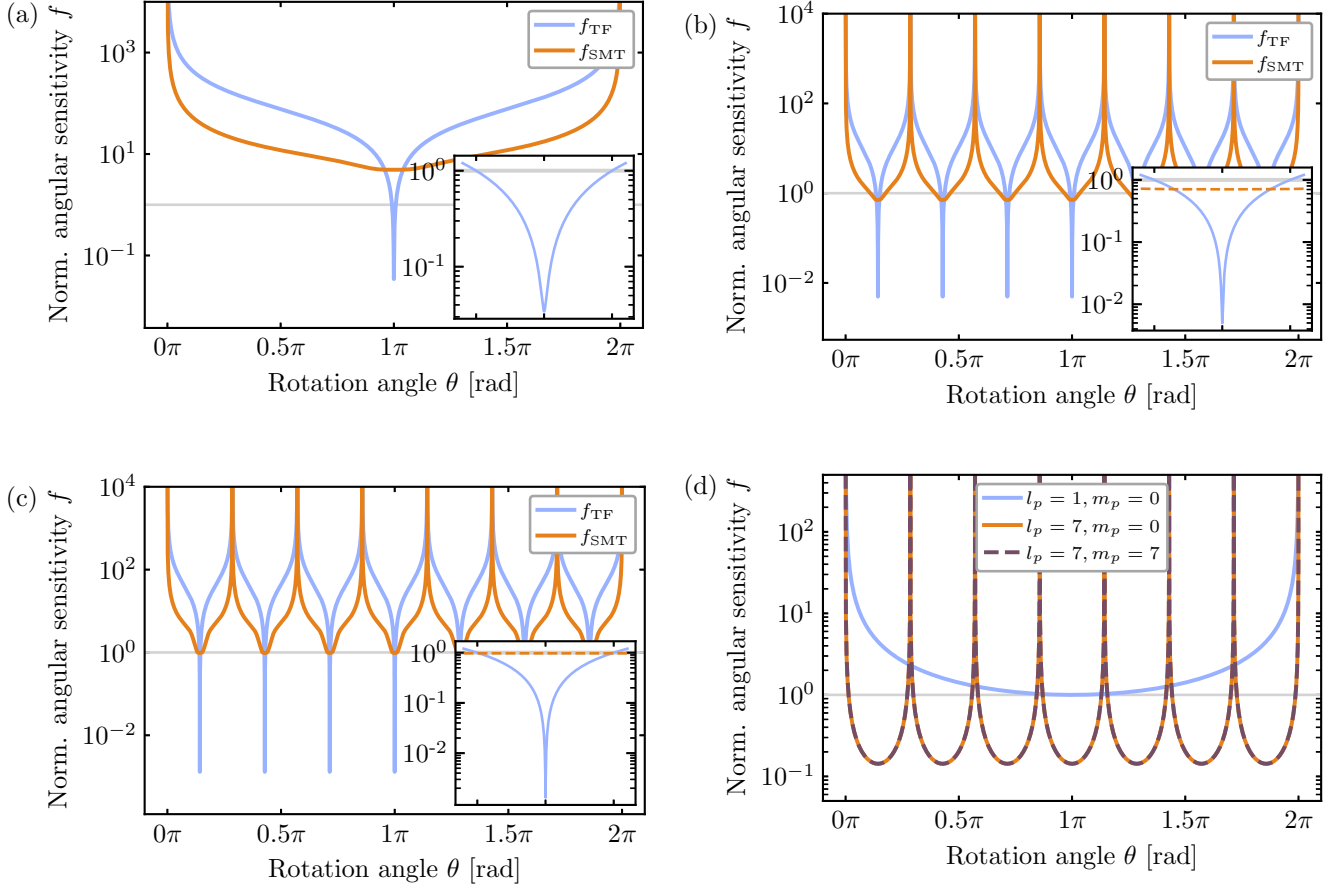


FIG. 11. Normalized angular displacement sensitivities f for the (a)-(c) medium-gain regime ($G_{\text{exp}} = 2$) and (d) low-gain regime ($G_{\text{exp}} = 0.01$). The pump parameters are (a) $l_p = 1, m_p = 0$; (b) $l_p = 7, m_p = 0$ and (c) $l_p = 7, m_p = 7$. In (a)-(c), the insets show the supersensitivity regions around $\theta = \pi$. Here, the outer x-axis ticks are located at the boundaries of the phase sensitivity region for the transfer-function approach. The widths (distances between the outer ticks) of said regions are (a) 52.1 mrad, (b) 53.3 mrad and (c) 13.1 mrad. Note that the line for f_{SMT} is dashed in the inset. In (d), for low-gain, f only depends on l_p and G and both f_{TF} and f_{SMT} coincide, see Eq. (4.27). For these figures, the average fitting constants A were used, as described in the text. In all plots, the horizontal thin gray line indicates the standard quantum limit $f = 1$.

following expression for the width of said region:

$$\Delta_{\text{TF}} = \frac{2\pi}{|l_p|} - \frac{4}{|l_p|} \arctan \left(\sqrt{\frac{1 + 4\frac{B}{A}}{2\mathcal{A}l_p^2(\Delta\theta_{\text{SNL}})^2 - 1}} \right). \quad (4.33)$$

Note that a supersensitivity region of nonzero width only exists for $2\mathcal{A}l_p^2(\Delta\theta_{\text{SNL}})^2 > 1$, which is equivalent to $(\langle \hat{N}_{s,\text{tot}}^{(1)} \rangle / K^{(1)} + 1) l_p^2 > 1$ and therefore always true for $l_p \neq 0$ and $G > 0$. Figure 14 shows the width of the supersensitivity region for selected values of l_p and m_p as a function of the experimental gain G_{exp} . Clearly, the width of the supersensitivity region decreases strongly with increasing gain.

For the low-gain limit, we find:

$$\lim_{G_{\text{exp}} \searrow 0} \Delta_{\text{TF}} = \begin{cases} 0 & l_p = \pm 1; \\ \frac{2\pi}{|l_p|} - \frac{4}{|l_p|} \arctan \left(\frac{1}{\sqrt{l_p^2 - 1}} \right) & |l_p| > 1, \end{cases} \quad (4.34)$$

which explains the behavior of the curves shown in Fig. 14 near $G_{\text{exp}} = 0$. Note that the first case does not contradict the above statement regarding the existence of a supersensitivity region of nonzero width, since it only applies in the limit $G_{\text{exp}} \searrow 0$. Figure 15 shows a plot of Eq. (4.34) and indicates that in the low-gain regime the supersensitivity region width is maximized for $l_p = 2$. Furthermore, even for large values of $|l_p|$, this width still remains much larger compared to the observed widths in the high-gain regime, leading to an interesting interplay between the gain value and the pump OAM value to simultaneously achieve both high angular sensitivity and

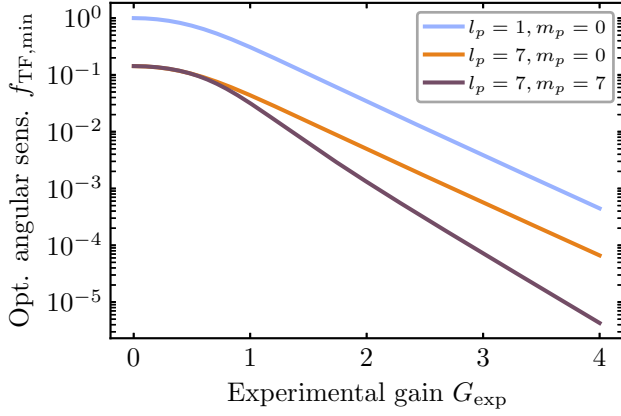


FIG. 12. Optimal (minimal) SNL-normalized angular sensitivity $f_{\text{TF},\text{min}}$ over the experimental gain G_{exp} as given by Eqs. (4.20a)–(4.20c) and (4.29) for selected values of l_p and m_p . As $G_{\text{exp}} \searrow 0$, $f_{\text{TF},\text{min}}$ approaches $1/|l_p|$, see Eq. (4.31).

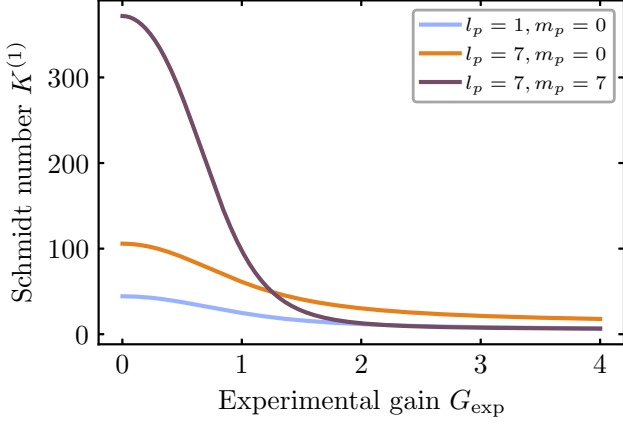


FIG. 13. Schmidt number $K^{(1)}$ as defined in Eq. (3.4) for the first crystal's high-gain eigenvalues $\Lambda_{mn}^{(1)}$. In the low-gain regime, the values for $l_p = 7$ coincide with the one presented in Fig. 1 (a small deviation is expected since we use averaged values for the fitting constant A in this section, as discussed in the text). At increasing gain, highly populated modes are amplified more strongly, leading to a strong reduction in the effective number of modes¹¹. Therefore, for $l_p = m_p = 7$, the number of effective modes may fall below $K^{(1)}$ for $l_p = 7$, $m_p = 0$ at high gain, even though it is much larger for low gain.

a wide supersensitivity region. Here, Figs. 12 and 14 can serve as guidelines to determine optimal points.

The behavior of $\Delta\theta_{\text{SMT}}$ [Eq. (4.26)] is less straightforward than $\Delta\theta_{\text{TF}}$. It is not immediately obvious that the expression is minimized for the same rotation angles as $\Delta\theta_{\text{TF}}$ [$\theta = \pi(2n+1)/l_p$ for $n \in \mathbb{Z}$], although this is suggested by Fig. 11. However, after normalization with

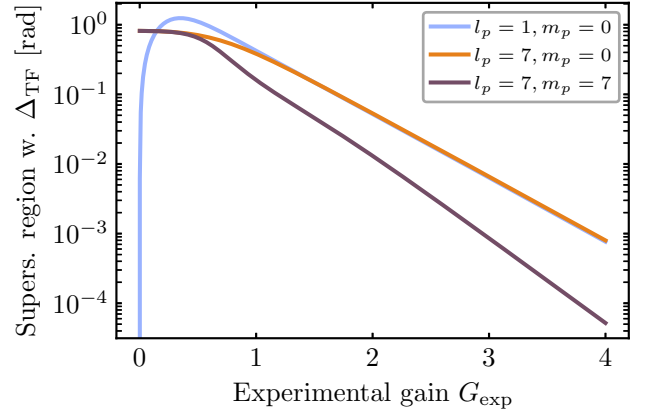


FIG. 14. Supersensitivity region width Δ_{TF} over the experimental gain G_{exp} for selected values of l_p and m_p . Evidently, the width of the region decreases rapidly with increasing gain. As G_{exp} approaches 0, the width only depends on l_p , see Eq. (4.34). For any $l_p \notin \{-1, 0, 1\}$, the width starts at a finite, nonzero value, while for $l_p = \pm 1$, it is exactly 0, meaning the phase supersensitivity region quickly degenerates into a single point as the gain decreases.

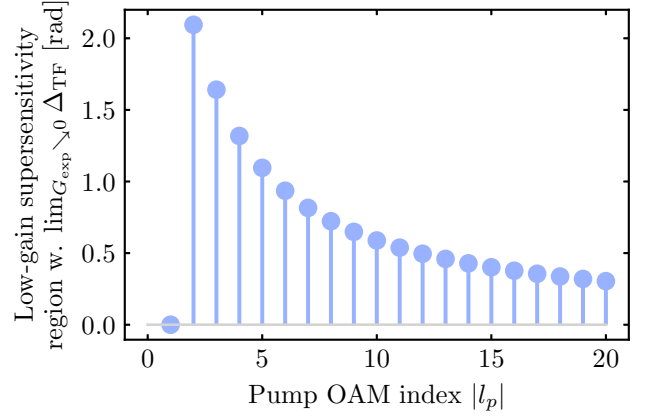


FIG. 15. Low-gain limit of the supersensitivity region width $\lim_{G_{\text{exp}} \searrow 0} \Delta_{\text{TF}}$ as given by Eq. (4.34). For $l_p = 0$, $\Delta\theta_{\text{TF}}$ and Δ_{TF} are undefined, as discussed in the text, while for $|l_p| = 1$, the supersensitivity region is given by a single point (zero width) for $G_{\text{exp}} \searrow 0$. Furthermore, for $|l_p| = 2$ the value is maximized with $\lim_{G_{\text{exp}} \searrow 0} \Delta_{\text{TF}} = \frac{2\pi}{3} \text{ rad} \approx 2.09 \text{ rad}$.

respect to the SNL, one can show that

$$\lim_{\theta \rightarrow \frac{\pi(2n+1)}{l_p}} \frac{df_{\text{SMT}}^2}{d\theta} = 0, \quad (4.35)$$

which implies that f_{SMT} has a local extremum as $\theta \rightarrow \pi(2n+1)/l_p$, since $df_{\text{SMT}}^2/d\theta = 2f_{\text{SMT}} df_{\text{SMT}}/d\theta$ and $f_{\text{SMT}} \neq 0$ for any θ . Moreover, at the mentioned extremal

point⁶,

$$f_{\text{SMT},\min} \stackrel{\text{def.}}{=} \lim_{\theta \rightarrow \frac{\pi(2n+1)}{l_p}} f_{\text{SMT}} = \frac{\sqrt{\langle \hat{N}_{s,\text{tot}}^{(1)} \rangle}}{G |l_p|}, \quad (4.36)$$

and as we show below, $f_{\text{SMT}} > f_{\text{SMT},\min}$ for $\theta \neq \pi(2n+1)/l_p$.

Indeed, one can perform the estimation:

$$\sum_{mn} \sinh^2 \left[4G \sqrt{\lambda_{mn}} \cos \left(\frac{l_p}{2} \theta \right) \right] \geq \left\{ \sum_{mn} \sqrt{\lambda_{mn}} \sinh \left[4G \sqrt{\lambda_{mn}} \left| \cos \left(\frac{l_p}{2} \theta \right) \right| \right] \right\}^2 \quad (4.37a)$$

$$> \sin^2 \left(\frac{l_p}{2} \theta \right) \left\{ \sum_{mn} \sqrt{\lambda_{mn}} \sinh \left[4G \sqrt{\lambda_{mn}} \left| \cos \left(\frac{l_p}{2} \theta \right) \right| \right] \right\}^2, \quad (4.37b)$$

where in the first line the Cauchy-Schwarz inequality²⁸, p. 31 has been applied and the normalization of the eigenvalues has been used ($\sum_{m,n} \lambda_{mn} = 1$), while in the second line, it has been assumed that $\sin^2 \left(\frac{l_p}{2} \theta \right) < 1$ meaning $\theta \neq \pi(2n+1)/l_p$, where $n \in \mathbb{Z}$. According to Eq. (4.26), this proves that $f_{\text{SMT}} > f_{\text{SMT},\min}$ and $f_{\text{SMT},\min}$ is indeed the global minimum of f_{SMT} .

Finally, note that the predicted optimal phase sensitivity for the transfer function approach always (except at $G = 0$) surpasses the phase sensitivity for the Schmidt mode theory: $f_{\text{TF},\min} < f_{\text{SMT},\min}$. To see this, one can first expand the $\Lambda_{mn}^{(1)}$ up to the second term and finds for the total intensity of the first crystal:

$$\langle \hat{N}_{s,\text{tot}}^{(1)} \rangle = \sum_{m,n} \Lambda_{mn}^{(1)} = G^2 + \frac{G^4}{3k} + \mathcal{R}(G), \quad (4.38)$$

where $k = \left(\sum_{m,n} \lambda_{mn}^2 \right)^{-1} > 0$ is the low-gain Schmidt number (defined using the low-gain Schmidt eigenvalues λ_{mn}), analogously to the high-gain Schmidt number defined in Eq. (3.4), and $\mathcal{R}(G) > 0$ is the remainder term, which includes high-order G -terms. Then, for $G > 0$,

$$G < \sqrt{\langle \hat{N}_{s,\text{tot}} \rangle} < \sqrt{\mathcal{A}}, \quad (4.39)$$

which confirms the inequality $f_{\text{TF},\min} < f_{\text{SMT},\min}$.

V. CONCLUSION

We have presented a theoretical framework to describe the parametric down-conversion process pumped

by Laguerre-Gaussian beams. Our description is based on the Schmidt-mode approach and is valid for any radial and orbital pump number. From the perspective of Schmidt modes, we have analyzed the mode structure and eigenvalue distributions of the generated quantum light and found that increasing the orbital and radial pump numbers leads to a significant broadening of the eigenvalue distribution, which is centered around $l_p/2$.

Furthermore, we have investigated an SU(1,1) interferometer pumped by Laguerre-Gaussian beams and studied its properties depending on the distance between the two crystals. For any nonzero distance, we have surprisingly found a non-monotonic behavior in the eigenvalue distribution, which becomes more pronounced at the point of destructive interference (dark fringe). To explain this behavior, we have performed an analytical analysis based on the double-Gaussian approximation and found a complex interplay of Bessel functions of different orders that occurs for any nonzero distance and is responsible for this behavior. The observed non-monotonic behavior allows for configurations where PDC modes carrying OAM higher than the pump OAM l_p have the largest population. These modes can then be filtered by increasing the gain due to the repopulation of the eigenvalues¹¹. In turn, non-trivial eigenvalue distributions result in complex non-Gaussian shaped intensity spectra for both the low- and high-gain regimes.

Finally, we have analyzed the application of the SU(1,1) interferometer for the detection of angular displacement. For this, we have considered a rotated Dove prism placed between the two crystals of the SU(1,1) interferometer. To study the sensitivity of the angular displacement measurement, we have compared the Schmidt-mode and the transfer-function approaches. Both approaches are consistent for the low-gain regime, but result in different sensitivities in the case of high gain. This is a consequence of the way the angular displacement has

⁶ To evaluate this limit, one can apply L'Hospital's rule²⁸, p. 56 twice to the square of the third fraction in Eq. (4.26).

been implemented: Inside the two-photon amplitude for the Schmidt-mode theory and into the transfer functions of the second crystal in the transfer-function approach, respectively. In the low-gain regime, the angular sensitivity depends only on the orbital pump number, however, at high-gain, the radial pump number also strongly affects the angular sensitivity due to the repopulation of the modes¹¹. The angular sensitivity improves as the gain increases and thus the effective number of modes (both radial and orbital) is reduced. At the same time, the width of the supersensitivity region decreases quickly with increasing gain. However, the interplay between the gain value and the pump OAM value suggests a promising method to achieve both high angular sensitivity and a wide supersensitivity range.

ACKNOWLEDGEMENTS

We acknowledge financial support of the Deutsche Forschungsgemeinschaft (DFG) via Project SH 1228/3-1 and via the TRR 142/3 (Project No. 231447078, Subproject No. C10). We also thank the PC2 (Paderborn Center for Parallel Computing) for providing computation time.

AUTHOR DECLARATIONS

Conflict of Interest

The authors have no conflicts to disclose.

DATA AVAILABILITY

The data that support the findings of this study are available from the corresponding author upon reasonable request.

APPENDIX A: SUPPLEMENTARY FIGURES

1. 2D mode profiles

Figure 16 shows the modulus squared $|u_{mn}(q)|^2/q$ (intensity profile) of the Schmidt modes of the SU(1,1) interferometer normalized according to Eq. (2.20a) for $l_p = 7$, $m_p = 0$ and $d = 0.42$ cm. The Schmidt modes are obtained by decomposing the expansion coefficients $\chi_n(q_s, q_i)$ as defined in Eq. (2.19). As one can see, the modes do not resemble Laguerre-Gaussian profiles. This is a consequence of the interference happening inside the SU(1,1) interferometer leading to a new set of basis modes.

2. Modal weight distributions

Figure 17 shows the normalised ($\sum_{m,n} \Lambda'_{mn} = 1$) modal weights according to Eq. (2.40) for $l_p = 18$, $m_p = 0$ for the low-gain [Fig. 17(a)] and high-gain [Fig. 17(b)] regime for different distances between the crystals around the dark fringe point. In contrast to the case $l_p = 7$ and $m_p = 0$ which was presented in Sec. III B in Fig. 6, where we have found the highest populated mode $n = 11$ for the distances $d = 0.42$ cm and $d = 0.5$ cm, the highest populated modes we have found here for the case of $l_p = 18$ and $m_p = 0$ is $n = 22$ for the distance $d = 0.42$ cm and $n = 21$ for $d = 0.5$ cm. Also, in this case, the highest populated mode has a higher OAM than the pump OAM ($l_p = 18$).

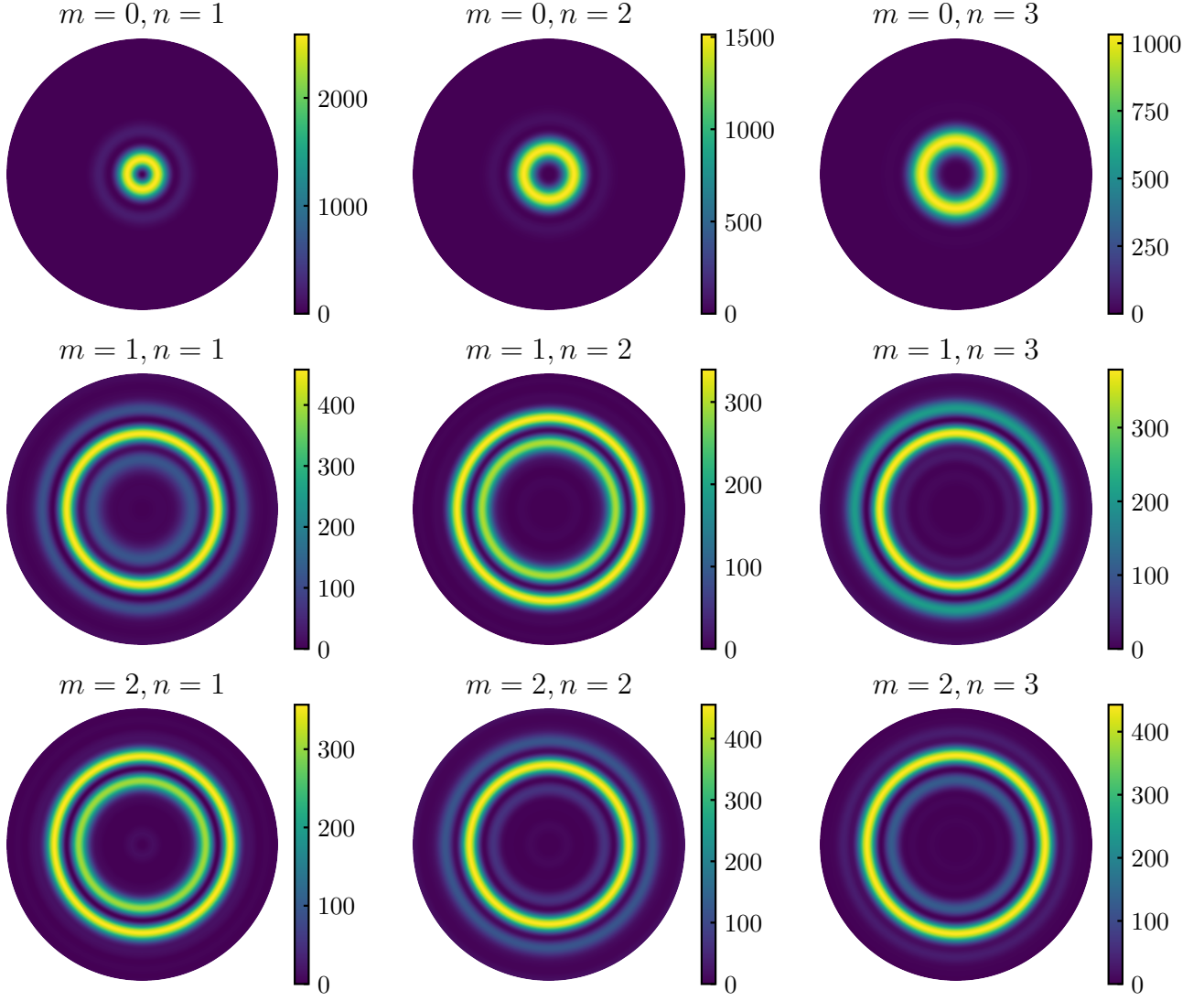


FIG. 16. Modulus squared $|u_{mn}(q)|^2/q$ (intensity profile) of the Schmidt modes of the SU(1,1) interferometer for $l_p = 7$, $m_p = 0$ and $d = 0.42$ cm. The radial mode index m ranges from 0 to 2, while the orbital index n ranges from 1 to 3. For an SU(1,1) interferometer, the modes are no longer similar to Laguerre-Gaussian modes.

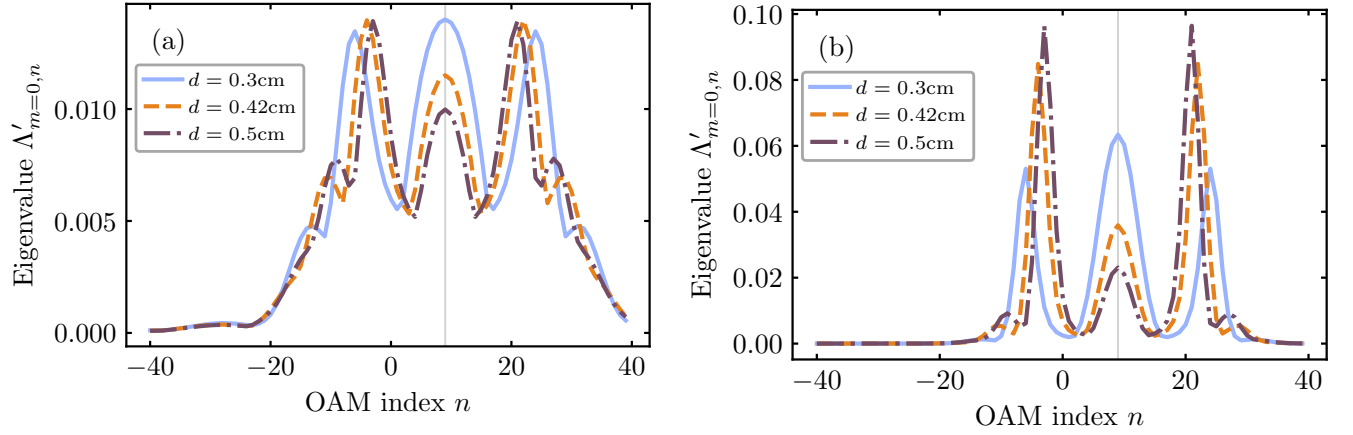


FIG. 17. Cuts of the normalized modal weights $\Lambda'_{m=0,n}$ ($\sum_{m,n} \Lambda'_{mn} = 1$) for $l_p = 18$, $m_p = 0$ for the (a) low-gain and (b) high-gain regime for different distances between the crystals around the dark fringe point. The thin gray lines indicate $n = l_p/2 = 9$. For the distance $d = 0.42\text{cm}$ the most populated OAM mode appears at $n = 22$, which is higher than the pump OAM $l_p = 18$. According to Eq. (2.40), the most populated OAM modes are strongly amplified in the high-gain regime, leading to a reshaping of the eigenvalue spectrum¹¹.

- ¹K. Y. Bliokh *et al.*, *Journal of Optics* **25**, 103001 (2023).
- ²A. Forbes, *Journal of Optics* **24**, 124005 (2022).
- ³L. Allen, M. W. Beijersbergen, R. J. C. Spreeuw, and J. P. Woerdman, *Phys. Rev. A* **45**, 8185 (1992).
- ⁴J. Wang, S. Chen, and J. Liu, *APL Photonics* **6**, 060804 (2021).
- ⁵A. Mair, A. Vaziri, G. Weihs, and A. Zeilinger, *Nature* **412**, 313 (2001).
- ⁶Y. Shen, X. Wang, Z. Xie, C. Min, X. Fu, Q. Liu, M. Gong, and X. Yuan, *Light Sci Appl* **8**, 90 (2019).
- ⁷A. Sit, F. Bouchard, R. Fickler, J. Gagnon-Bischoff, H. Larocque, K. Heshami, D. Elser, C. Peuntinger, K. Günthner, B. Heim, C. Marquardt, G. Leuchs, R. W. Boyd, and E. Karimi, *Optica* **4**, 1006 (2017).
- ⁸R. Fickler, R. Lapkiewicz, W. N. Plick, M. Krenn, C. Schaeff, S. Ramelow, and A. Zeilinger, *Science* **338**, 640 (2012).
- ⁹E. Karimi, S. A. Schulz, I. De Leon, H. Qassim, J. Upham, and R. W. Boyd, *Light Sci. Appl.* **3**, e167 (2014).
- ¹⁰Miatto, F.M., Brougham, T., and Yao, A.M., *Eur. Phys. J. D* **66**, 183 (2012).
- ¹¹P. Sharapova, A. M. Pérez, O. V. Tikhonova, and M. V. Chekhova, *Phys. Rev. A* **91**, 043816 (2015).
- ¹²L. Beltran, G. Frascella, A. M. Perez, R. Fickler, P. R. Sharapova, M. Manceau, O. V. Tikhonova, R. W. Boyd, G. Leuchs, and M. V. Chekhova, *Journal of Optics* **19**, 044005 (2017).
- ¹³R. F. Offer, D. Stulga, E. Riis, S. Franke-Arnold, and A. S. Arnold, *Commun Phys* **1**, 84 (2018).
- ¹⁴D. Cozzolino, D. Bacco, B. Da Lio, K. Ingerslev, Y. Ding, K. Dalgaard, P. Kristensen, M. Galili, K. Rottwitt, S. Ramachandran, and L. K. Oxenløwe, *Phys. Rev. Appl.* **11**, 064058 (2019).
- ¹⁵M. Krenn, J. Handsteiner, M. Fink, R. Fickler, R. Ursin, M. Malik, and A. Zeilinger, *Proc. Natl. Acad. Sci. U.S.A.* **113**, 13648 (2016).
- ¹⁶G. Xie, L. Li, Y. Ren, H. Huang, Y. Yan, N. Ahmed, Z. Zhao, M. P. J. Lavery, N. Ashrafi, S. Ashrafi, R. Bock, M. Tur, A. F. Molisch, and A. E. Willner, *Optica* **2**, 357 (2015).
- ¹⁷M. Hiekkamäki, F. Bouchard, and R. Fickler, *Phys. Rev. Lett.* **127**, 263601 (2021).
- ¹⁸A. K. Jha, G. S. Agarwal, and R. W. Boyd, *Phys. Rev. A* **83**, 053829 (2011).
- ¹⁹A. M. Pérez, T. S. Iskhakov, P. Sharapova, S. Lemieux, O. V. Tikhonova, M. V. Chekhova, and G. Leuchs, *Opt. Lett.* **39**, 2403 (2014).
- ²⁰M. Manceau, F. Khalili, and M. Chekhova, *New Journal of Physics* **19**, 013014 (2017).
- ²¹M. V. Chekhova and Z. Y. Ou, *Adv. Opt. Photon.* **8**, 104 (2016).
- ²²G. Frascella, E. E. Mikhailov, N. Takanashi, R. V. Zakharov, O. V. Tikhonova, and M. V. Chekhova, *Optica* **6**, 1233 (2019).
- ²³P. R. Sharapova, G. Frascella, M. Riabinin, A. M. Pérez, O. V. Tikhonova, S. Lemieux, R. W. Boyd, G. Leuchs, and M. V. Chekhova, *Phys. Rev. Res.* **2**, 013371 (2020).
- ²⁴B. Baghdasaryan, C. Sevilla-Gutiérrez, F. Steinlechner, and S. Fritzsche, *Phys. Rev. A* **106**, 063711 (2022).
- ²⁵S. Karan, S. Aarav, H. Bharadhwaj, L. Taneja, A. De, G. Kulkarni, N. Meher, and A. K. Jha, *Journal of Optics* **22**, 083501 (2020).
- ²⁶D. Klyshko, *Photons and Nonlinear Optics* (Taylor & Francis, New York, 1988).
- ²⁷F. Pampaloni and J. Enderlein, Gaussian, Hermite-Gaussian, and Laguerre-Gaussian beams: A primer (2004), [arXiv:physics/0410021](https://arxiv.org/abs/physics/0410021).
- ²⁸I. Bronshtein, K. Semendyayev, G. Musiol, and H. Mühlig, *Handbook of Mathematics* (Springer Berlin Heidelberg, 2015).
- ²⁹G. N. Watson, *A Treatise on the Theory of Bessel Functions* (Cambridge University Press, 1995).
- ³⁰Bateman Manuscript Project, H. Bateman, and A. Erdélyi, *Tables of Integral Transforms*, Vol. 2 (McGraw-Hill, 1954).
- ³¹N. K. Fontaine, R. Ryf, H. Chen, D. T. Neilson, K. Kim, and J. Carpenter, *Nat. Commun.* **10**, 1865 (2019).
- ³²D. Scharwald, T. Meier, and P. R. Sharapova, *Phys. Rev. Res.* **5**, 043158 (2023).
- ³³K. Y. Spasibko, T. S. Iskhakov, and M. V. Chekhova, *Opt. Express* **20**, 7507 (2012).
- ³⁴N. González, G. Molina-Terriza, and J. P. Torres, *Opt. Express* **14**, 9093 (2006).